Available online at www.sciencedirect.com
SCIENCE DIRECT
Geochimica et Cosmochimica Acta 70 (2006) 480–503
Geochimica
www.elsevier.com/locate/gca

Partial melting processes above subducting plates: Constraints from ^{231}Pa–^{235}U disequilibria

Simon Turner [a,b,*], Marcel Regelous [a], Chris Hawkesworth [a], Kia Rostami [a]

[a] Department of Earth Sciences, Wills Memorial Building, University of Bristol, Bristol BS8 1RJ, UK
[b] GEMOC, Department of Earth and Planetary Sciences, Macquarie University, Sydney, NSW 2109, Australia

Received 25 April 2005; accepted in revised form 7 September 2005

Abstract

The processes involved in the formation and transport of partial melts above subducting plates remain poorly constrained relative to those at mid-ocean ridges. In particular, ^{238}U–^{230}Th–^{226}Ra disequilibria, that might normally be used to constrain melting dynamics, tend to be swamped by the effects of fluid addition from the down-going plate. The ^{231}Pa–^{235}U system provides an exciting exception to this because the highly incompatible nature of Pa means that fractionation and in-growth during partial melting overwrite the effects of fluid U addition. We present ^{231}Pa–^{235}U data on 50 well-characterised lavas from seven subduction zones in order to examine partial melting processes. Measured ($^{231}Pa/^{235}U$) ratios are all >1 and 15% are >2. Overall ($^{231}Pa/^{235}U$) shows broad positive correlations with ($^{230}Th/^{238}U$) and La/Yb and negative trends against Ba/Th and ($^{226}Ra/^{230}Th$). These systematics can differ from arc to arc but suggest that ($^{231}Pa/^{235}U$) tends to be higher in sediment-rich arc lavas where the effects of fluid addition are muted and there is less of a ^{231}Pa deficit for melting to overprint. We have explored the effects of decompression melting, frictional drag dynamic melting with and without ageing subsequent to fluid U addition to the wedge as well as flux melting models. Globally, average ($^{231}Pa/^{235}U$) appears to correlate negatively with convergence rate and so in the numerical models we use the local subduction rate for the rate of matrix flow through the melting zone. Using this assumption and reasonable values for other parameters, the melting models can simulate the overall range of ($^{231}Pa/^{235}U$) and some of the data trends. However, it is clear that local variations in some parameters, especially source composition and extent of melting, exert a major influence on ^{231}Pa–^{235}U disequilibria. Some data, which lie at a high angle to the modelled trends, may be explained by mixing between small degree hydrous melts formed near the slab and larger degree, decompression melts produced at shallow depth.

1. Introduction

Understanding the way in which partial melting occurs within the Earth is crucial to models for heat transfer and plate tectonics as well as to the study of volcanism in general. At mid-ocean ridges, adiabatic decompression provides a simple and physically robust melting model and U-series disequilibria data have been used to constrain the rates at which the up-welling and melting occur as well as the threshold porosity at which melt is expelled from the mantle matrix (McKenzie, 1985; Spiegelman and Elliott, 1993). At subduction zones, U-series data have provided a wealth of information on the timing and mechanisms of fluid addition from the descending plate because of the preferential mobility of U and Ra relative to Th in oxidising, aqueous fluids (see Turner et al., 2003 for a recent review). Nevertheless, in contrast to mid-ocean ridges, much less is known about the processes of partial melt formation at subduction zones, despite their importance in both the formation and recycling of crustal materials.

In general, whereas mid-ocean ridge basalts (MORB) are characterised by excesses of ^{230}Th over ^{238}U, which can be linked to ^{230}Th in-growth during partial melting (see Lundstrom, 2003 for a recent review), any such melting signal in subduction zones is usually obscured by addition of U from the subducting plate which contributes >80% of the total U budget in most arc lavas (Fig. 1). These lavas

* Corresponding author. Fax: +61 2 9850 6904.
E-mail address: sturner@els.mq.edu.au (S. Turner).

0016-7037/$ - see front matter © 2005 Elsevier Inc. All rights reserved.
doi:10.1016/j.gca.2005.09.004

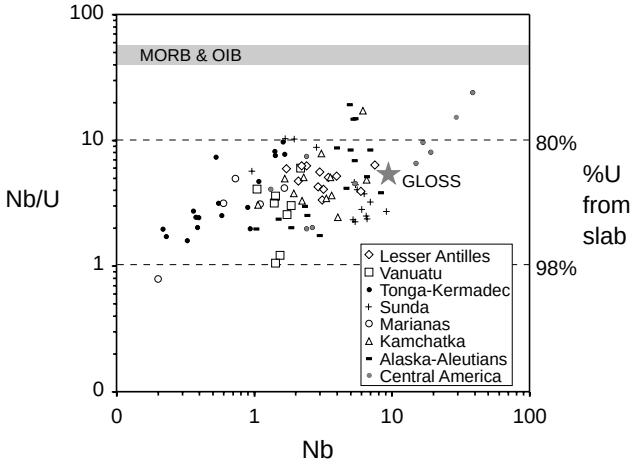

Fig. 1. Pa is inferred to behave similarly to Nb in terms of fluid solubility and incompatibility during mantle melting (cf. Turner et al., 2003) and this Nb/U versus Nb diagram highlights the fact that 80–98% of the U in most arc lavas is derived from the subducting plate (see Fig. 2B). The range in Nb reflects the opposing effects of prior depletion of the mantle wedge and addition of Nb by the sediment contributions. MORB and OIB average is taken from Hofmann et al. (1986) and GLOSS is the composition of average global subducting sediment from Plank and Langmuir (1998).

most typically preserve ^{238}U excesses, arguably developed over an integrated time of several 10s kyr (see Bourdon et al., 2003a,b; Turner et al., 2003 and Peate and Hawkesworth, 2005 for recent discussion) and by analogy would be predicted to have excesses of ^{235}U over ^{231}Pa (for which Nb provides the closest analogue). Therefore, the observation that most subduction zone lavas in fact have $(^{231}\text{Pa}/^{235}\text{U}) > 1$ is of fundamental importance because it suggests that, for this U-series nuclide pair, the effects of partial melting almost always overprint those of fluid addition (Bourdon et al., 1999; Dosseto et al., 2003; Pickett and Murrell, 1997; Thomas et al., 2002). This can be partially understood in terms of experimental and theoretical partitioning data (Blundy and Wood, 2003) which predict that $D_{\text{Pa/U}} \sim 10^{-3}$, compared with $D_{\text{Th/U}}$ which will be close to 1 for mineral assemblages is likely to occur in the mantle wedge above the down-going plate. Nevertheless, none of these elements are sufficiently compatible for straightforward batch or fractional partial melting to produce the observed degrees of disequilibria for likely extents of melting and so the ^{231}Pa excesses (as well as any ^{230}Th excesses) require a melting process which allows for in-growth (see Elliott, 1997). This requires that the mantle should not be static but rather the matrix move through the melting region remaining above its solidus for ~1 Myr (McKenzie, 1985; Spiegelman and Elliott, 1993). Once melts are formed, the preservation of large, fluid-derived ^{226}Ra excesses in the erupted lavas suggests that melt segregation and transport to the surface are highly efficient and occur in channels at 100–1000s of metres per year (Turner et al., 2001).

In summary, there is general agreement that ^{231}Pa–^{235}U systematics provide unique insights into partial melting processes above subducting plates. However, there remain many uncertainties as to the details of the process and until now comprehensive measurements of ^{231}Pa–^{235}U disequilibria have been available from only a few localities (Bourdon et al., 1999; Dosseto et al., 2003; Thomas et al., 2002). Thus, in order to constrain better the processes of partial melting above subducting plates, we have undertaken ^{231}Pa–^{235}U analyses of 50 new lavas encompassing seven additional arcs.

2. Sample details, analytical techniques, and results

Exceptionally well-characterised lavas from the Lesser Antilles, Vanuatu, Mariana, Sunda, Alaska-Aleutian, and Kamchatka arcs were chosen for analysis to significantly expand the available published database. All have previously been analysed for ^{238}U–^{230}Th–^{226}Ra disequilibria by thermal ionisation mass spectrometry and additional sample information, comprehensive geochemical and isotopic data, and details of analytical techniques are available in the references cited in Table 1. Several new samples from Tonga were also analysed to expand the geographic coverage available within that unique arc.

Details of the ^{231}Pa analysis techniques employed here have been described in detail elsewhere (Regelous et al., 2004). In brief, samples were spiked with a ^{233}Pa tracer, which was milked from a ^{237}Np solution, and then dissolved using standard HF–HCl–HNO_3 methods. Protactinium was separated from the bulk of the rock matrix on anionic exchange resin in HF–HCl and subsequently cleaned of high field strength elements, transition metals, and U and Th using TRU Spec resin. Atomic ^{231}Pa/^{233}Pa ratios were measured on a ThermoFinnigan Neptune multicollector, inductively coupled plasma mass spectrometer at the University of Bristol by peak switching on a secondary electron multiplier, using admixed U of known isotopic composition to correct for instrumental mass bias and fluctuations in beam intensity (Regelous et al., 2004). The internal precision on analyses of solutions containing about 50–100 fg of Pa was typically 0.4–0.7% (2σ), and the external reproducibility of the method, determined by repeat analysis of rock samples, is better than 1.5%. Each batch of ^{233}Pa spike prepared was calibrated against the rock standard TML, which is widely used as an equilibrium standard for U series nuclides, including the ^{231}Pa–^{235}U pair. The accuracy of this method of calibration was assessed by determining ^{235}U and ^{231}Pa concentrations in several rock samples, which are known to be older than 0.8 Ma and therefore in ^{231}Pa–^{235}U equilibrium. These measurements that are presented in Regelous et al. (2004) were performed at the same time as the analyses reported here and indicate that ^{231}Pa concentrations can be measured with an accuracy that is within the reproducibility of the measurements. Activity ratios were calculated using previously published U concentrations and assuming $\lambda_{235} = 9.849 \times 10^{-10}\ \text{y}^{-1}$ and $\lambda_{231} = 2.116 \times 10^{-5}\ \text{y}^{-1}$ based on the half-lives compiled by Bourdon et al. (2003a,b).

Table 1
Protactinium analyses of subduction zone lavas

Arc/volcano	Sample #	Age (AD or years)	SiO_2 (wt%)	Th (ng/g)	U (ng/g)	^{231}Pa (fg/g)	$(^{231}Pa/^{235}U)$[a]	Sources of supporting data for the same samples $^{*226}Ra$ data in Turner et al. (2001)
Lesser Antilles								
Statia	SE8228	8250 bp	54.68	0.574	0.290	179.2	1.900	Turner et al. (1996)*
St. Kitts	K369	40,000 bp	52.35	0.778	0.384	183.7	1.417	Turner et al. (1996)*
St. Kitts	Kit50	200	51.80	0.687	0.353	183.3	1.596	Turner et al. (1996)*
Montserrat	MVO244	1998	60.17	2.447	0.783	331.1	1.300	Zellmer et al. (2003)*
Martinique	M8225	1929	60.26	2.225	0.686	306.5	1.374	Turner et al. (1996)*
St. Vincent	STV354	1979	52.90	1.052	0.534	364.6	2.099	Turner et al. (1996)*, Heath et al. (1998)
St. Vincent	STV371	1590	54.81	0.851	0.443	307.1	2.131	Turner et al. (1996)*, Heath et al. (1998)
Ile de Caille	RW 33	1000 bp	47.91	2.051	0.763	657.2	2.648	Turner et al. (1996)*
Ile de Caille	RW 35	1000 bp	47.19	1.624	0.679	501.5	2.271	Turner et al. (1996)*
Grenada	GDA014	<10 kyr	47.89	2.576	1.185	454.0	1.178	Turner et al. (1996)*
Vanuatu								
Aoba	68611	<10 kyr	47.81	1.262	0.443	204.3	1.418	Turner et al. (1999)*
Ambrym	AMB-26	<2 kyr	51.25	0.928	0.365	142.7	1.202	Turner et al. (1999)*
Lopevi	Bomb	1970	50.35	0.561	0.259	110.5	1.312	Turner et al. (1999)*
Karua	KB-19	<10 kyr	51.10	0.636	0.399	135.5	1.044	Turner et al. (1999)*
Tanna	Yas 1975	1975	54.93	2.376	1.364	472.8	1.066	Turner et al. (1999)*
Tanna	Yas 1993	1993	55.98	2.226	1.278	588.9	1.417	Turner et al. (1999)*
Matthew	68553	1940	61.96	1.620	0.682	439.4	1.981	Turner et al. (1999)*
Matthew	68557	1940	63.24	1.314	0.620	390.3	1.935	Turner et al. (1999)*
Tonga								
Tafahi	TAF45/7	Recent	51.97	0.107	0.072	32.5	1.388	Turner et al. (1997, 2000)
Late	Late 7	1790-1854	53.19	0.136	0.111	40.1	1.111	Turner et al. (1997, 2000)
Ata	482-8-3	Recent	53.20	0.417	0.189	89.6	1.457	Turner et al. (1997, 2000)
Sunda								
Galunggung	64LG	1982	49.01	0.672	0.163	87.8	1.656	Turner and Foden (2001)*
Rindjani	LBK/86/2	1900	53.74	4.273	1.150	439.9	1.176	Turner and Foden (2001)*
Tambora	T205/88	1815	55.45	11.857	3.370	1488.0	1.357	Turner and Foden (2001)*
Sangeang Api	SA2	1985	48.35	6.802	1.690	995.7	1.811	Turner and Foden (2001)*
Ija (Flores)	FL26	1900	51.79	0.439	0.170	138.0	2.496	Turner and Foden (2001)*
Marianas								
Pagan	PA1	1981	51.54	0.620	0.253	134.3	1.632	McDermott and Hawkesworth (1991), Woodhead (1989)*
Guguan	GU6	1883	51.97	0.360	0.191	97.8	1.574	McDermott and Hawkesworth (1991), Woodhead (1989)*
Uracas	U4	1952	57.85	0.960	0.355	185.7	1.608	McDermott and Hawkesworth (1991), Woodhead (1989)*
Kamchatka								
Sheveluch	2562	1964	58.20	1.228	0.676	284.2	1.292	Turner et al. (1998)*
Tolbachik	T889	1976	50.40	1.134	0.707	331.9	1.443	Turner et al. (1998)*
Bakening	BAK32	2000 bp	66.00	3.225	1.660	807.4	1.495	Turner et al. (1998)*
Karymsky	J4497	1976	62.40	1.692	1.005	451.9	1.382	Turner et al. (1998)*
Karymsky	J4499	1971	62.20	1.603	0.968	451.5	1.434	Turner et al. (1998)*
Avachinsky	A4-91	1991	55.90	0.639	0.349	194.5	1.713	Turner et al. (1998)*
Gorely	G574	600 bp	52.30	0.873	0.392	214.5	1.682	Turner et al. (1998)*
Alaska-Aleutians								
Spurr	92JBS02	1992	56.64	0.872	0.250	178.1	2.190	George et al. (2003)
Spurr	85CNS17	1953	54.89	1.430	0.349	254.4	2.241	George et al. (2003)
Redoubt	90CNR12	1989	63.44	1.826	0.754	424.1	1.729	George et al. (2003)
Katmai	97ND02	1912	55.16	1.642	0.759	359.0	1.454	George et al. (2003)
Ukinrek	UK-25B	1977	48.98	1.529	0.579	347.5	1.845	George et al. (2003)
Pavlof	PAV-86	1996	53.15	0.816	0.448	192.7	1.322	George et al. (2003)
Shishaldin	99 SH 08	1999	49.28	1.257	0.808	429.8	1.635	George et al. (2003)
Akutan	96PS23	1978	55.37	1.673	0.900	419.0	1.431	George et al. (2003)
Bogoslof	Bog 1796	1796	61.00	4.814	2.112	1294.8	1.885	George et al. (2003)
Seguam	99SJP01	Historic	52.66	0.900	0.512	232.7	1.397	George et al. (2003)
Kasatochi	K81-7Aa	1899	49.07	1.078	0.617	746.2	3.718	George et al. (2003)
Kanaga	KAN 5-8a	1900	53.65	3.497	1.663	842.1	1.557	George et al. (2003)
Little Sitkin	52-496	1900	58.63	2.458	1.097	540.6	1.515	George et al. (2003)
Kiska	Kiska 62	1962	55.22	1.936	0.936	412.5	1.355	George et al. (2003)

[a] Activity ratios based on $\lambda_{235} = 9.849 \times 10^{-10}$ and $\lambda_{231} = 2.116 \times 10^{-5}$.

Since nearly all of the samples have ^{226}Ra excesses (including the non-historic samples RW33, Taf45/7, and 482-8-3), none of the ^{231}Pa data were age corrected.

The new data show considerable variation within each subduction zone (Table 1) and expand the known range of ($^{231}Pa/^{235}U$) ratios in arc lavas to something more akin to that observed in MORB (1.5–3.5), although the average arc value of 1.65 ± 0.47 (excluding Kasatochi; see below) is significantly lower than the average MORB value (2.53 ± 0.62). When combined with published data (Bourdon et al., 1999; Dosseto et al., 2003; Pickett and Murrell, 1997), the ($^{231}Pa/^{235}U$) ratios range from 1.18 to 2.65 in the Lesser Antilles, 1.04 to 1.98 in Vanuatu, 0.81 to 1.69 in Tonga–Kermadec, 1.18 to 2.50 in the Sunda arc, 1.61 in the Marianas, 1.22 to 1.71 in Kamchatka, and 1.32 to 2.24 in the Aleutians. The lava from Kasatochi in the Aleutians yielded a ($^{231}Pa/^{235}U$) ratio of 3.72 which represents the highest ($^{231}Pa/^{235}U$) ratio yet measured from any arc and is similar to the highest ratios observed in MORB (Lundstrom et al., 1999). Unfortunately, no material remained available to check this result and so this analysis is not included in most of the diagrams plotted. Published data from Nicaragua and Costa Rica in central America (Thomas et al., 2002) have ($^{231}Pa/^{235}U$) ratios ranging from 1.26 to 1.77.

3. Global ^{231}Pa–^{235}U systematics

The combined global arc dataset is presented in the plot of ($^{231}Pa/^{235}U$) versus ($^{230}Th/^{238}U$) in Fig. 2A along with the field for MORB. We consider initially the effects of fluid addition, of ageing since fluid addition, the consequences of sediment subduction and of partial melting. As discussed below, the five samples from the southern Lesser Antilles have very high ($^{231}Pa/^{235}U$) at moderate to low ($^{230}Th/^{238}U$). These include the sample from Kick 'em Jenny which is anomalous in most datasets for having very low ($^{230}Th/^{238}U$) compared with those of samples from adjacent volcanoes. Interestingly, the Iya sample from the Sunda arc is similar to that from Kick 'em Jenny in having very low ($^{230}Th/^{238}U$) compared with the rest of that arc and this is the sample with the highest ($^{231}Pa/^{235}U$) and lowest ($^{230}Th/^{238}U$). If these six samples are considered as a separate group in Fig. 2A (and also in Figs. 3A and 4C), then the rest of the global dataset form a broad, largely positively sloped array which lies largely above ($^{231}Pa/^{235}U$) = 1 and spreads to both sides of the ($^{230}Th/^{238}U$) = 1 line, as originally observed by Pickett and Murrell (1997). Thomas et al. (2002) identified sub-parallel tiers within their central American data in this diagram, but our data reveal that the slope of the data arrays in the ($^{231}Pa/^{235}U$)–($^{230}Th/^{238}U$) diagram can vary significantly from arc to arc (see Section 5).

Recent addition of U by fluids will result in a vector directed towards the origin as shown in Fig. 2A and because the half-life of ^{230}Th (~76 kyr) is more than twice that of ^{231}Pa (~33 kyr) any ageing subsequent to fluid U addition results in a curved path back towards the equipoint (see Fig. 2A). The displacement above this vector then provides a measure of the combined effects of partial melting and/or any elapsed time between fluid U addition

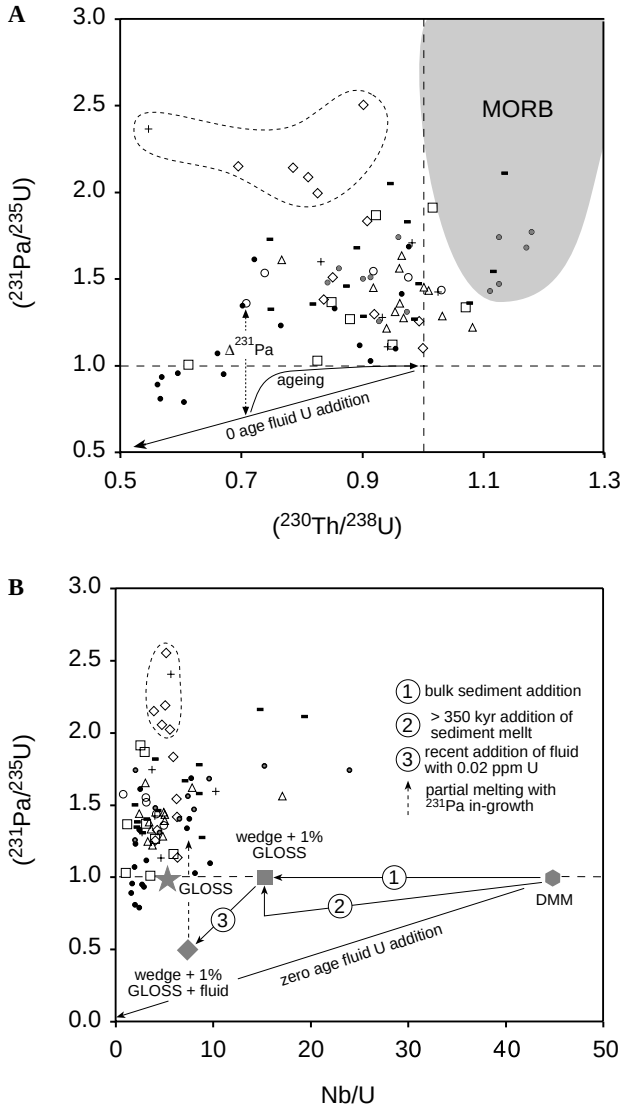

Fig. 2. (A) Plot of ($^{231}Pa/^{235}U$) versus ($^{230}Th/^{238}U$) with data from island arc lavas. The equipoint occurs at the intersection of the two dashed lines which identify secular equilibrium in each parent-daughter system. Vectors show the sense of displacement due to fluid addition and partial melting ($\Delta^{231}Pa$). Dashed field identifies the anomalous samples from the southern Lesser Antilles and the Iya sample from the Sunda arc. MORB field from Lundstrom (2003). (B) Plot of ($^{231}Pa/^{235}U$) versus Nb/U ratio with mass balance vectors to show that much of the total U added to the wedge (cf. Fig. 1) occurred >100 kyr ago, most likely in the form of sediment. We assume this is either added as bulk sediment (path 1) or as a U-enriched melt sufficiently long ago that the mantle has returned to secular equilibrium (path 2). Recent addition of 0.02 ppm U by fluids (path 3) results in ($^{231}Pa/^{235}U$) ~0.5 superimposed upon which is the effect of ^{231}Pa in-growth during partial melting which leads to ($^{231}Pa/^{235}U$) > 1. DMM is the depleted MORB mantle source composition from Salters and Stracke (2004) and GLOSS is the composition of average global subducting sediment from Plank and Langmuir (1998). Data from Table 1, Pickett and Murrell (1997), Bourdon et al. (1999), Dosseto et al. (2003), and Thomas et al. (2002).

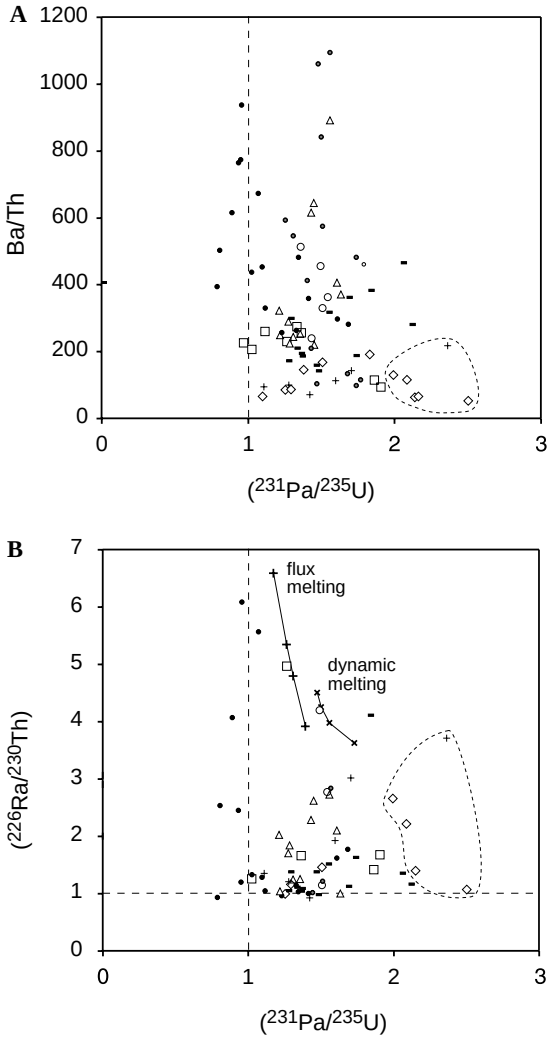

Fig. 3. (^{231}Pa/^{235}U) plotted against (A) Ba/Th and (B) (^{226}Ra/^{230}Th) including the results of illustrative ageing + dynamic melting and flux melting calculations (parameters as for the Lesser Antilles in Table 3). Data sources and symbols as in Fig. 2.

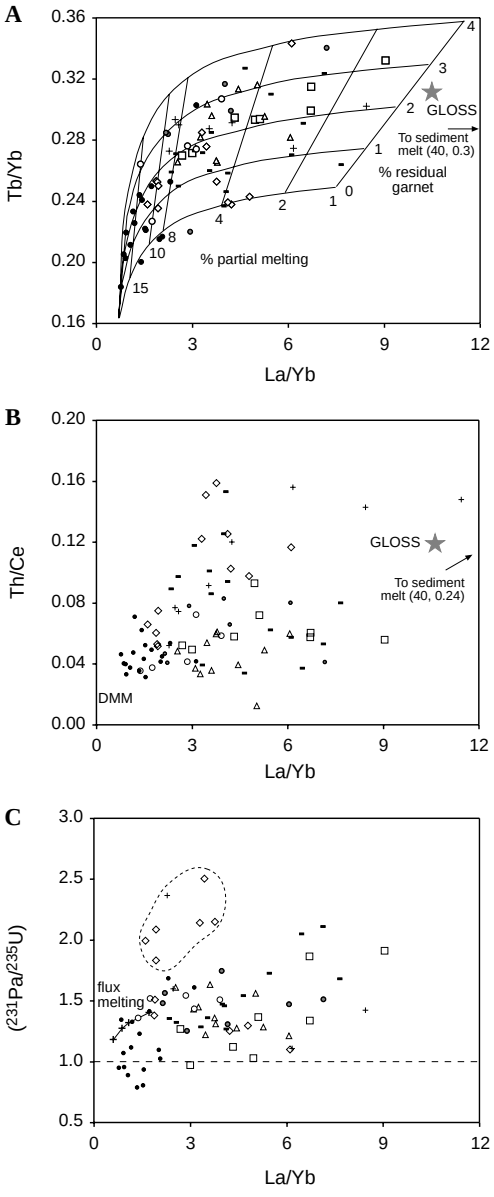

Fig. 4. (A) Plot of Tb/Yb versus La/Yb contoured for extent of fractional partial melting and amount of residual garnet assuming the DMM source composition of Salters and Stracke (2004) and the modal mineralogy and partition coefficients given in Table 2. The melting mode was olivine 0.2, orthopyroxene 0.2, clinopyroxene 0.4, and garnet/spinel 0.2. (B) Plot showing the broad positive correlation between Th/Ce and La/Yb for arc lavas from which it is inferred that much of the variation in La/Yb may be attributed to sediment addition. A 10% melt of typical pelagic sediment has La/Yb = 40, Tb/Yb = 0.3, and Th/Ce = 0.24, assuming the bulk partition coefficients determined by Johnson and Plank (1999). (C) Plot of La/Yb versus (^{231}Pa/^{235}U) along with results from an illustrative flux melting simulation (other parameters as for the Lesser Antilles in Table 3). Dashed line identifies the anomalous samples from the southern Lesser Antilles and the Iya sample from the Sunda arc. Data sources and symbols as in Fig. 2 (note that potassic lavas inferred to reflect low degrees of melting from Sangeang Api and Tambora in the Sunda arc have La/Yb > 12 and lie beyond the region plotted).

and partial melting on the (^{231}Pa/^{235}U) ratio. We assume that melting often has much less effect upon (^{230}Th/^{238}U) ratios in arcs (but see George et al., 2003) since $D_{U/Th}$ is close to 1 in clinopyroxene at depths of 80–100 km near the slab (we assume $D_{Th/U} = 0.8$ based on Landwehr et al., 2001) and garnet is unlikely to be a major residual phase for these rocks (see below). Note also that, if the duration of ageing since fluid U addition is a couple of half-lives of ^{231}Pa or more, then the measured (^{231}Pa/^{235}U) ratio, rather than the displacement above the fluid addition line in Fig. 2A, may more accurately isolate the displacement due to melting. In contrast, it has been argued that for most lavas from Tonga there has been little ^{231}Pa–^{235}U fractionation during melting due to an absence of residual clinopyroxene and so the displacement of these samples above the fluid addition line (see Fig. 2A) has been inferred to reflect 50–60 kyr of ageing since fluid addition of U (Bourdon et al., 1999). The effects of fluid addition and melting will be harder to deconvolve if fluid addition and melting are coupled (e.g., Bourdon et al., 2003a,b; Thomas et al., 2002). Either way, excluding most of the lavas from Tonga, all samples analysed have

(^{231}Pa/^{235}U) > 1 and so partial melting effects appear to be observable in the ^{231}Pa–^{235}U systematics of almost all arc lavas.

It should be stressed that only some fraction of the U enrichment in arc lavas identified in Fig. 1 is due to recent fluid addition or recorded by U-series disequilibria. This is highlighted in the plot of (^{231}Pa/^{235}U) versus Nb/U in Fig. 2B. If all of the decrease in Nb/U ratio in the arc lavas were due to recent fluid addition of U, then the (^{231}Pa/^{235}U) ratios of the subduction modified wedge prior to partial melting would lie between 0.05 and 0.25. None of the available melting models could achieve the measured (^{231}Pa/^{235}U) ratios of 0.8–2.5 from such low starting ratios, assuming parameters appropriate to melting beneath arcs (see below). However, many studies of arc lavas have argued for a three component mass balance (e.g., Ellam and Hawkesworth, 1988; McDermott et al., 1993) which includes addition of ⩽1% sediment to the wedge as well as the fluid component assumed responsible for ^{238}U excesses (e.g., Elliott et al., 1997; Hawkesworth et al., 1997; Regelous et al., 1997; Turner et al., 1997). As illustrated in Fig. 2B, the consequence of ~1% sediment addition is to reduce the Nb/U ratio of the mantle wedge from 45, a value typical of the MORB or OIB (ocean island basalt) source (Hofmann et al., 1986), down to 14. In contrast, we assume there is no net effect on (^{231}Pa/^{235}U) either because sediment was added without fractionating (^{231}Pa/^{235}U) or because it occurred sufficiently long ago that any U-series disequilibria have since returned to secular equilibrium (e.g., Bourdon et al., 1999; Elliott et al., 1997; George et al., 2003, 2005; Turner et al., 1997). More recent addition of as little as 0.02 ppm U by fluids further lowers the Nb/U ratio of this source to 7 and results in (^{231}Pa/^{235}U) ratios between 1 and 0.5, comparable to those implied from the 1:1 U-addition vector in Fig. 2A. Superimposed upon the final composition of this multiply metasomatised mantle wedge is the effect of ^{231}Pa in-growth during partial melting which leads to increases in (^{231}Pa/^{235}U) which typically overprint any fluid related U-excesses and result in (^{231}Pa/^{235}U) ratios >1 (Fig. 2B).

The preceding discussion emphasises that the amount of U from the slab inferred from Nb/U is much greater than that from U–Th disequilibria, and for that reason the data require at least two steps of U addition of different ages, with much of the U being added at least several 100 kyr ago in a component that may have been dominated by contributions from subducted sediment. In Fig. 2A, the global array is broadly parallel to the fluid addition vector and so the (^{231}Pa/^{235}U) ratios are inversely correlated with the relative effects of fluid addition as reflected in the (^{230}Th/^{238}U) ratio. Elevated Ba/Th ratios are also often regarded as a hallmark of fluid addition in subduction zone lavas due to the orders of magnitude greater fluid-mobility of Ba relative to that of Th (Brenan et al., 1995) and there is also a weak negative array between Ba/Th and (^{231}Pa/^{235}U) at the global scale (Fig. 3A). Disequilibria between ^{226}Ra and ^{230}Th can be extreme in arc lavas and tend to be positively correlated with fluid indices like Ba/Th. This has been attributed to addition of Ra by the last increments of fluid addition and rapid melt extraction (Turner et al., 2001). Although there is no clear correlation between (^{231}Pa/^{235}U) and (^{226}Ra/^{230}Th), Fig. 3B does suggest that the highest (^{231}Pa/^{235}U) ratios are found in those samples with the lower (^{226}Ra/^{230}Th) and vice versa.

If the source composition were known, trace element ratios can be inverted to constrain the total extent of melting. Such an approach is used in Fig. 4A which shows the range in Tb/Yb and La/Yb resulting from melting of the depleted MORB source (DMM) composition of Salters and Stracke (2004). At face value, the results suggest that the majority of arc lavas analysed for ^{231}Pa reflect moderate to large (4–15%) degrees of partial melting, consistent with their major element chemistry. However, the rare earth element abundances in the mantle wedge will also be affected by the addition of sediment which will increase La/Yb and Tb/Yb such that the estimates from Fig. 4A should be treated as minimum constraints on the extent of melting. Elevated Tb/Yb can result from melting in the presence of residual garnet and the contours in Fig. 4A also provide a maximum constraint on the likely amount of residual garnet for the arc lavas (⩽4%). However, we do not believe that garnet is a residual phase during melting in the wedge, but rather that the elevated La/Yb and Tb/Yb ratios can be attributed to sediment addition (see below). Furthermore, a number of studies (e.g., Class et al., 2000; Elliott et al., 1997; Hawkesworth et al., 1997; Johnson and Plank, 1999) have found evidence that the sediment component is added as a partial melt in equilibrium with residual garnet and an accessory phase(s) such as allanite (Plank, 2005) which preferentially retain high field strength elements such as Nb (and by analogy Pa) and Th over U (as implied in Fig. 2B for example). Model 10% melts of average global subducting sediment (GLOSS) using the bulk partition coefficients from Johnson and Plank (1999) have La/Yb = 40 and so have significant leverage in Fig. 4. Consequently, these garnet signatures are likely to be derived from the slab and we suggest that most of the arc lavas studied reflect 8–15% partial melting (cf. Pearce and Parkinson, 1993) with little or no residual garnet in the mantle wedge (potassic lavas from Sangeang Api and Tambora are probable exceptions to the latter constraint). In any case, despite garnet being the one mantle phase in which $D_{Pa/U}$ is predicted to be >0.01 (Blundy and Wood, 2003), even the maximum amounts of residual garnet allowed by Fig. 4A have a negligible effect upon bulk $D_{Pa/U}$.

In Fig. 4B there is a very broad positive correlation between La/Yb and Th/Ce, the latter index being sensitive to sediment addition (Hawkesworth et al., 1997). This supports the preceding arguments that at least some of the variation in La/Yb is related to sediment or sediment melt (Th/Ce = 0.24) addition and, if the southern Lesser Antilles samples and the Iya sample from Flores are again considered as a separate group, there is also a broad positive correlation between (^{231}Pa/^{235}U) and La/Yb (and Tb/Yb

not shown) in Fig. 4C. Such correlations might be used to infer a link between ^{231}Pa–^{235}U disequilibria and the integrated extent of partial melting (cf. Fig. 4A). Instead, the key to understanding these correlations may be that the more sediment-rich sources (higher La/Yb and Th/Ce) are less sensitive to the effects of addition of a relatively constant amount of U by fluids because they had higher Th and U concentrations to begin with (Elliott et al., 1997; Hawkesworth et al., 1997; McDermott and Hawkesworth, 1991; Regelous et al., 1997; Turner et al., 1997). Consequently, these sources suffer the least displacement along the U addition vector in Fig. 2A so that the effects of partial melting have less of a deficit of ^{231}Pa relative to ^{235}U to overprint. Thus, partial melting leads to higher absolute ($^{231}Pa/^{235}U$) ratios from more sediment-rich, higher ($^{230}Th/^{238}U$) sources and contours for a constant partial melting effect in Fig. 2A are parallel to the fluid addition vector (see Fig. 17c in Turner et al., 2003). This is in contrast to MORB and OIB where the slopes of arrays in ($^{231}Pa/^{235}U$) versus ($^{230}Th/^{238}U$) space reflect the clinopyroxene/garnet ratio in the source (Bourdon and Sims, 2003). By analogy lower Ba/Th and ($^{226}Ra/^{230}Th$) ratios are found in samples from the more sediment-rich, fluid-insensitive sources and these start with higher ($^{231}Pa/^{235}U$) ratios before melting leading to the broadly negative correlations in Fig. 3.

In principle, the effects of any ageing between the time of U fluid addition and partial melting should be distinguishable. However, this has proved difficult in practice. Ageing will reduce the slope of any correlations in Figs. 2A, 3A, and 4C and so it may be that the extent to which any such ageing can be identified relies on the ability to discern slopes on these diagrams within individual arcs and this is explored in further detail below.

4. Models for partial melting in the mantle wedge

Whereas the main controls on stable trace element ratios are source composition and residual mineralogy, bulk partition coefficients, and the integrated extent of partial melting, U-series isotope ratios are also affected by the time scale of melting. For example, batch melting models require degrees of partial melting less than 1% in order to obtain ($^{231}Pa/^{235}U$) ratios >1.5, and since such small degrees of melting are unlikely for arc magmas (cf. Fig. 4A) this indicates that in-growth models are *required* to explain the arc lava data. Assuming very rapid melt extraction (see below), the key factor in such models is the velocity at which the matrix passes through the melting region because this determines the amount of time available for U-series nuclide in-growth (see Elliott, 1997, and Lundstrom, 2003, for overviews). One end-member in-growth melting model produces disequilibria via continuing chromatographic equilibration with peridotite wall-rocks as the melt ascends large distances (and over time periods of 10s kyr) via porous flow (Spiegelman and Elliott, 1993). However, at subduction zones the rapid channelled melt transport inferred from ^{226}Ra systematics (Sigmarsson et al., 2002; Turner et al., 2001) suggests that such interaction will be minimal and is unlikely to be the origin of the ^{231}Pa excesses in arc lavas (Bourdon et al., 2003a,b; Dosseto et al., 2003; Turner et al., 2003). Accordingly, most recent models for arc lavas have invoked some variation on the theme of dynamic melting involving protracted melt production but fast melt extraction using the numerical treatment of McKenzie (1985) and Williams and Gill (1989).

At mid-ocean ridges, the mantle flows upwards due to plate separation and so this has provided the incentive to relate the matrix flow rate inferred from U-series disequilibria to physical observables such as axial spreading rate (see Lundstrom, 2003, for a recent review). The situation is less straightforward in arcs and an outstanding question concerns the nature of matrix flow through the melting zone that is recorded by the ^{231}Pa excesses. There are a range of possible physical models which would result in dynamic melting in the mantle wedge and in Fig. 5 we illustrate three we have chosen to explore quantitatively in the remainder of this paper. All three assume that melt ascent is effectively instantaneous.

4.1. Decompression dynamic melting

Major and trace element data as well as the temperatures and volatile contents of some arc lavas have long been used to argue for a component of decompression melting beneath arcs (e.g., Parkinson and Arculus, 1999; Pearce and Parkinson, 1993; Plank and Langmuir, 1988; Sisson and Bronto, 1998). Upwelling might occur because small density and viscosity contrasts arising from the addition of volatiles and the presence of partial melt are sufficient to cause gravitational instabilities leading to localised, diapiric, peridotite upwelling (Brémond d'Ars et al., 1995; Gerya and Yuen, 2003). Alternatively, recent dynamic modelling has shown that implementation of temperature-dependent viscosity leads to a component of upward flow beneath arcs (Furukawa, 1993; Kincaid and Sacks, 1997; van Keken et al., 2002) which could lead to decompression melting (Conder et al., 2002) as illustrated in Fig. 5A. This might be accentuated by extensional tectonics within the arc or back-arc. An attraction of this model is that it can reconcile evidence that at least some arc magmas last equilibrated with mantle peridotite at high temperatures at low pressures (e.g., Elkins Tanton et al., 2001). During decompression melting, ^{231}Pa excesses would be controlled by both the rate of upwelling and length of the melting column (Bourdon et al., 1999) which will be influenced by crustal thickness (e.g., Plank and Langmuir, 1988). Note that the use of the term "melt column" simply refers to the along-flow dimension of the melting region and does not imply a vertical column. It is not clear how peridotite migrating along the upwelling convection limb would have received the metasomatic signature of sediment (melt) and fluid addition that is characteristic of arc lavas, and dynamic melts of unmetasomatised wedge material

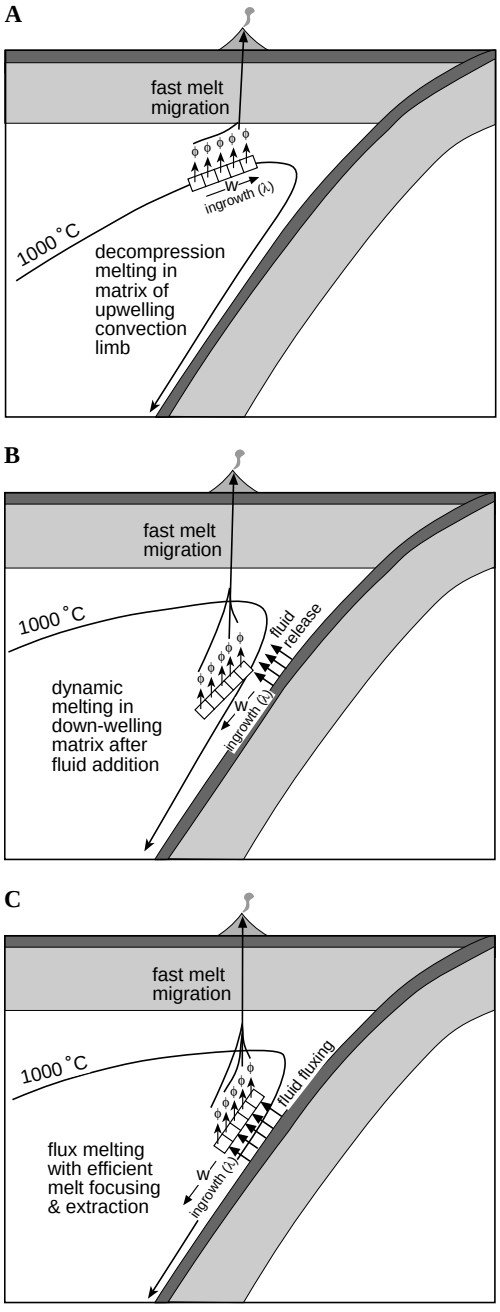

Fig. 5. Illustrations of the different melting models investigated in this study. In (A), partial melting occurs predominantly in response to decompression along the upwelling limb of convection in the mantle wedge. In (B), partial melting occurs as mantle wedge material that has been hydrated during prior (up-dip) episodes of fluid addition crosses the hydrous peridotite solidus. The models shown in (A) and (B) are analogous to an inclined dynamic MORB melting column in which the matrix enters the melting region and melt is extracted in a stepwise fashion whenever the melt fraction exceeds the threshold porosity (ϕ). Each parcel of matrix flows through the melting region at velocity (W) and U-series nuclide in-growth occurs between each extraction step in proportion to W and the relevant decay constant (λ). In (A), the length of the melting column is limited by the thickness of the overlying lithosphere, whereas in (B) a primary control on the extent of U-series disequilibria produced is W which will be controlled by the local rate of convergence. The flux melting model of Thomas et al. (2002) is illustrated in (C) where fluid addition and partial melting are coupled in a synchronous continuum and in-growth again occurs between each step. Note that in all three models the melt column is inclined and we use of the term "melt column" to refer to the along-flow dimension of the melting region.

might be expected to resemble MORB unless mixed with deeper, hydrous melts (see Section 7). Nevertheless, many back-arc lavas do have elevated H_2O contents and preserve ^{238}U excesses (e.g., Peate et al., 2001; Stolper and Newman, 1994).

4.2. Frictional drag melting with or without ageing since fluid U addition

It has long been recognised that frictional drag against the subducting plate will induce downward directed convection in the wedge, at least close to the wedge–plate interface. In the second model illustrated (Fig. 5B), ^{231}Pa ingrowth reflects the rate of downward convection through a region where partial melting is occurring as this motion translates hydrated peridotite across its solidus. It is assumed that fluid addition lowers the peridotite solidus but that this hydrated peridotite does not melt until convection drags it across its solidus. In other words, the onset of melting is controlled by the location of an isotherm (England et al., 2004; Tatsumi et al., 1986) and continues because material is translated obliquely across the isotherms into increasingly hotter parts of the wedge.

The simplest numerical simulation of this model is shown in Fig. 6 employing diagrams to be used in Appendix A and subsequent sections, and which, along with Fig. 7, illustrate the effects of varying the principal variables in the models. The model involves dynamic melting of a variably metasomatised mantle wedge using extended versions of the equations presented by Williams and Gill (1989). The source region is composed of peridotite that has been enriched by sediment (melt) addition at some stage in the past but is assumed to be in secular equilibrium prior to fluid addition. We simulate this enriched source by three increments of addition of a fluid with a fixed composition (see Fig. 6). The thin lines in Fig. 6 show the resultant compositions after 10% dynamic melting of this range of source compositions and that those sources with a greater relative fluid contribution achieve the lowest ($^{231}Pa/^{235}U$) and ($^{230}Th/^{238}U$) ratios after melting. The double-headed arrow indicates the effect of varying the degree of melting of the 30 ppb U source to 8 or 15%.

A variation of this model allows for ageing of the metasomatised wedge after U addition by fluids (e.g., Tatsumi et al., 1986). We have inferred the duration of this ageing from the slope of arrays in the U–Th equiline diagram as discussed in the references listed in Table 1. Note that these ages are inferred to reflect the integrated age of fluid U addition rather than any discrete event and that this is assumed not to affect ^{226}Ra which is inferred to reflect the final stages of fluid addition (Turner et al., 2000). This aged source then undergoes 10% dynamic melting and so we refer to this model as "ageing + dynamic melting." The Nb-normalised "isochron" diagram of Bourdon et al. (1999) in Fig. 6C is utilised here because it most clearly illustrates the multi-stage evolution simulated by the "ageing + dynamic melting" model. Note that the ageing + dynamic melting

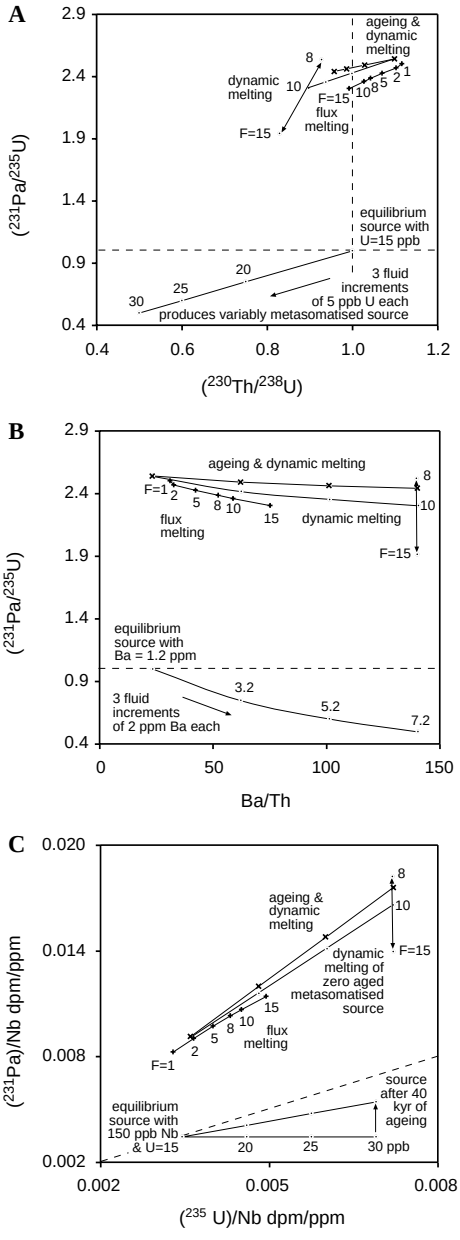

Fig. 6. Plots of (A) (^{231}Pa/^{235}U) versus (^{230}Th/^{238}U), (B) (^{231}Pa/^{235}U) versus Ba/Th, and (C) (^{231}Pa)/Nb versus (^{235}U)/Nb to illustrate the various melting models investigated. The source region is composed of peridotite that has been enriched by sediment (melt) addition at some stage in the past but is assumed to be in secular equilibrium prior to fluid addition. In the dynamic melting models, this enriched source is then metasomatised by three increments of addition of a fluid with a fixed composition (5 ppb U, 2 ppm Ba). The thin line shows the composition after 10% dynamic melting of this range of source compositions and the double-headed arrow indicates how the composition of the 30 ppb source melt would vary if the extent of melting were 8 or 15%. The "ageing and dynamic melting" line shows the results of dynamic melting of the same source (X's along the curve indicate the same range of initial source compositions) after it has undergone 40 kyr ageing since fluid U addition (see source composition after 40 kyr ageing on (C)). The flux melting curve shows the results of calculations based on the model presented by Thomas et al. (2002) and has the total extent of melting (F) indicated in %. The relevant parameters for the models shown in Figs. 6 and Fig. 11–18 are given in Tables 2 and 3 (see text for discussion).

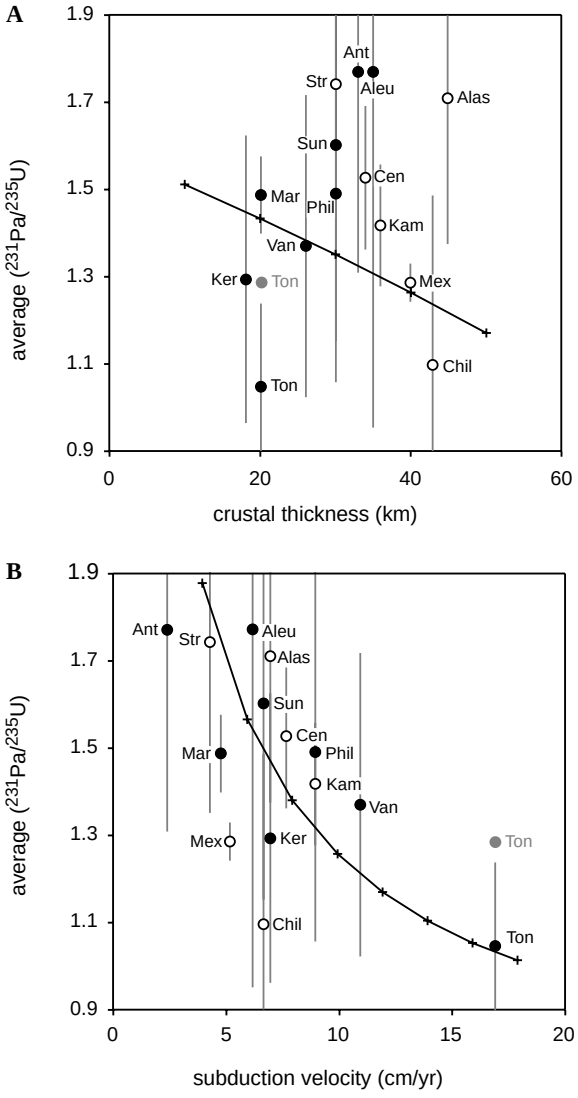

Fig. 7. Plots of average (^{231}Pa/^{235}U) for lavas from individual arcs versus (A) crustal thickness (compiled from Clift and Vannucchi, 2004; Plank and Langmuir, 1988) and (B) subduction velocity (from the compilation in Plank and Langmuir, 1998). Vertical grey lines represent 1 standard deviation of the variation within each arc (Tonga, Ton; Kermadec, Ker; Philippines, Phil; Aleutians, Aleu; Mariana, Mar; Vanuatu, Van; Lesser Antilles, Ant; Sunda, Sun; Stromboli, Str; Alaska, Alas; Central America, Cen; Kamchatka, Kam; Sth. Chile, Chil; Mexico, Mex). The grey circle for Tonga represents the average of samples with (^{231}Pa/^{235}U) ratios >1 from this arc. Also shown are the results for a dynamic melting simulation based on the equations of Williams and Gill (1989) with variable matrix flow (i.e., subduction) rate (W) and the following fixed parameters: bulk partition coefficient for U = 0.0058 and Pa = 2.2×10^{-6} based on Blundy and Wood (2003), extent of melting $F = 0.15$, porosity $\phi = 0.002$, and melting column base = 100 km. The source composition was assumed to have initially been in secular equilibrium with a U concentration of 0.00514 ppm. To simulate the island arc environment, this was enhanced by variable addition of U by fluids 30 kyr prior to partial melting leading to the following range of compositions at the time of melting: U = 0.00514–0.02014 ppm; (^{231}Pa/^{235}U) = 1–0.435. The plotted values of (^{231}Pa/^{235}U) are the average (^{231}Pa/^{235}U) ratio for this range of source compositions. The model in (A) varies the crustal thickness (top of the melt column) and assumes a constant matrix velocity (subduction rate) of 5 cm/yr. The model in (B) varies the matrix velocity and assumes a constant top for the melting column of 20 km.

model could in principle apply to the decompression model in Fig. 5A as well. As Figs. 6A and B show, the primary effect of ageing for several 10s kyr is to elevate and reduce the range in (^{231}Pa/^{235}U) ratios and the slope of the curves in the (^{231}Pa/^{235}U) versus (^{230}Th/^{238}U) and (^{231}Pa/^{235}U) versus Ba/Th diagrams.

4.3. Flux melting

The third model illustrated in Fig. 5C is flux melting. The basic distinction of this model is the assumption that the continuum of dehydration reactions occurring in the subducting plate (Poli and Schmidt, 1995; Schmidt and Poli, 1998) directly induces melting each time they are injected into the wedge so that small melt fractions are produced for each increment of fluid addition and then coalesce (Bourdon et al., 2003a,b; Dosseto et al., 2003; Thomas et al., 2002). Melting continues in this model because fluid is continually being added. Since the wedge is convecting and melt is extracted as soon as the critical threshold porosity (often referred to as the residual porosity) is exceeded, ^{231}Pa in-growth occurs in the down-dragged matrix between each increment of fluid addition and is again linked to the rate of downward convection. The flux melting simulation employed here uses the calculations described in detail in Thomas et al. (2002), although Th and Pa are assumed to be fluid immobile (see Section 6). Because the variations produced in fluid mobile element concentrations and U-series nuclide in-growth are linked to the number of iterative fluid addition and melting episodes, these parameters are strongly correlated with the overall summed extent of partial melting. Thus, in these models, the lowest (^{231}Pa/^{235}U) and (^{230}Th/^{238}U) ratios result from the largest degrees of partial melting (see Fig. 6).

4.4. Links with physical observables

In all of the models described above, the extent of ^{231}Pa in-growth should be linked to the rate of matrix transfer. For the latter two models, especially, this is likely to be controlled by the local subduction rate assuming that there is strong coupling between the descending plate and convection in the mantle wedge (but see also Turner and Hawkesworth, 1997; Honda and Yoshida, 2005). However, in the case of the decompression model, ^{231}Pa in-growth may also be influenced by extensional tectonics and the length of the melt column which would imply a potential link with crustal thickness. Therefore, in a first order attempt to try to discriminate between these models we have plotted the average (^{231}Pa/^{235}U) ratios for each subduction zone against crustal thickness and the velocity of the subducting plate in Fig. 7.

A hint of a positive correlation between (^{231}Pa/^{235}U) and crustal thickness was found by Bourdon et al. (2003a,b) and Turner et al. (2003) using the early dataset of Pickett and Murrell (1997). Our new dataset shows that a broad positive correlation exists between average (^{231}Pa/^{235}U) and crustal thickness for oceanic arcs (although there are a wide range of values within each arc, Fig. 7A), and that the opposite is observed for arcs built upon continental crust. Thus, there is no simple global correlation with crustal thickness. A seemingly better global correlation emerges between average (^{231}Pa/^{235}U) ratios and the velocity of the subducting plate in Fig. 7B. Although the correlation is largely controlled by data from Tonga, where (^{231}Pa/^{235}U) ratios <1 are thought to reflect a lack of residual clinopyroxene during melting (Bourdon et al., 1999), a reasonable correlation still exists if only the Tonga samples with (^{231}Pa/^{235}U) ratios >1 are averaged (see Fig. 7B).

Since the matrix flow rate and melting column length are key variables in all dynamic melting models, it is possible to forward model possible relationships in Fig. 7 using a dynamic melting simulation (e.g., Williams and Gill, 1989) and reasonable input parameters for the other variables such as extent of melting, melt column length, residual porosity, bulk partition coefficients, and source composition. The results also serve to illustrate the effects of varying melt column length and matrix flow rate whilst keeping all other parameters constant. The curve in Fig. 7A shows that increasing crustal thickness (i.e., decreasing the length of the melting column) at constant matrix flow and melting rate leads to a trend of decreasing average (^{231}Pa/^{235}U) with increasing crustal thickness. This is the opposite slope to that defined by the oceanic arcs. A positive correlation would require that the melting rate or total extent of melting also decreased with increasing crustal thickness but, as we discuss in Section 6, there appears to be little evidence for this. In contrast, continental arcs do form a negative slope but one which has a much steeper trend than the model results. Nevertheless, it is not clear why the extent of melting would vary with crustal thickness in oceanic arcs yet remain constant beneath continental arcs or why the continental arcs are not systematically displaced to higher (^{231}Pa/^{235}U) than the oceanic arcs. In summary, there does not appear to be any convincing evidence that crustal thickness plays a first order control on ^{231}Pa–^{235}U systematics at a global scale. Instead, the trend in global averages is in much better agreement with the modelled decreases in (^{231}Pa/^{235}U) that result from increasing the matrix flow rate (i.e., subduction velocity) at a constant melt column length (Fig. 7B).

5. Variations within subduction zones

A caveat to the treatment in Fig. 7 is that the use of average (^{231}Pa/^{235}U) ratios hides both the large variations present within each arc, and proposed differences in the controlling mineralogy, as in Tonga and the southern Lesser Antilles. Accordingly we have also examined the variations within each individual subduction zone in detail (see Appendix A), since each arc has a number of different tectonic attributes which might be anticipated to link to partial melting processes. In particular, we have subdivided

the different arcs according to their slope in the (^{231}Pa/^{235}U) versus (^{230}Th/^{238}U) diagram. A positive slope may imply relatively little elapsed time between fluid addition of U and partial melting, and that the slope is largely determined by fluid addition, whereas a horizontal slope, as observed in central America (Thomas et al., 2002), or a negative slope requires more complex models.

Although the data trends are often scattered and may require further analyses to firm up in some instances, it is apparent from Appendix A and Figs. 11–18 that there are significant intra-arc differences in ^{231}Pa–^{235}U behaviour. In the (^{231}Pa/^{235}U) versus (^{230}Th/^{238}U) diagram, only Vanuatu and the Alaska-Aleutian arcs form positive trends; Tonga is also positive but that is because the fluid addition signal has not been overprinted by the effects of melting due to the inferred absence of residual clinopyroxene (Bourdon et al., 1999). In comparison, the Mariana, Kermadec, and central American suite form roughly horizontal (^{231}Pa/^{235}U)–(^{230}Th/^{238}U) trends (Figs. 12 and 16; Bourdon et al., 1999; Thomas et al., 2002) whereas the northern Lesser Antilles, Kamchatka, and possibly Sunda arcs show negative trends.

In presenting the data we also explore the applicability of the dynamic, dynamic + ageing, and the flux melting models described above and use the (^{231}Pa/^{235}U) versus (^{230}Th/^{238}U) and (^{231}Pa/^{235}U) versus Ba/Th diagrams from Fig. 6 to facilitate direct comparisons (the possible role for decompression melting will be revisited in Section 7). Because the rate of matrix flow is likely to be linked to subduction rate in all of the models considered here (cf. Fig. 5) and arguably correlates with average (^{231}Pa/^{235}U) in Fig. 7B, we have taken the local subduction rate to be indicative of this matrix flow rate. U, Ba, and Ra are assumed to be fluid mobile whereas Th and Pa are not (but see Section 6). In an effort to permit fair comparison of these three different models, we have attempted to make all common parameters (e.g., partition coefficients, mantle mineralogy, etc.) identical. These and the other key parameters used for each arc are listed in Tables 2 and 3.

6. Comparison of the partial melting models

Overall, the models do a poor job in simulating the data which, admittedly, are often scattered. Although the positions of the model curves can be moved around in Figs. 11–18 by varying some of the input parameters in Table 3, their general orientation will remain unaltered. Thus, for example, the positive (^{231}Pa/^{235}U)–Ba/Th trends in the Vanuatu, Sunda, and Alaska-Aleutian arcs cannot be simulated. In the Lesser Antilles, no model can reproduce the data from the northern islands and in Vanuatu the ageing + dynamic melting models provide reasonable fits to some of the data but cannot replicate the data from Matthew or the apparent positive trend formed by the other islands in Fig. 14. This emphasises that large differences in (^{231}Pa/^{235}U) ratios within several individual arcs, such as the Lesser Antilles and Vanuatu, are difficult to replicate without significant changes in melting parameters. In the Sunda arc, for example, the significantly higher (^{231}Pa/^{235}U) ratio of the Iya sample compared with the other arc front volcanoes could be reproduced by lowering the extent of melting, residual porosity or increasing the length of the melting region but there is no independent evidence for this (see also Section 7). To the contrary in fact, the (^{231}Pa/^{235}U) ratios are lower at Sangeang Api and Tambora where the extent of melting is arguably lower (cf. Fig. 4A). Implicit in all of the models is that the source region is homogeneous on the scale of 100s km, yet Fig. 4 highlights that most arcs also show evidence for significant variations in local source composition (variable depletion, sediment amount/composition, and Indian vs Pacific wedge material) which must play a role in addition to variations in the melting parameters. In summary, it is clear that local as well as global variations in critical parameters must exert a major influence on ^{231}Pa–^{235}U disequilibria.

The different models discussed all have physical plausibility but the general lack of coherent data trends means that it is not easy to distinguish between them in Figs. 11–18. The effect of ageing subsequent to fluid U addition, typically for 10s–1000s of years prior to melting, arguably better simulates the data in the Nb-normalised diagrams for the Vanuatu, Sunda, Mariana, and Kamchatka arcs. This is consistent with inferences about the significance of inclined U–Th arrays generally (Bourdon et al., 2003a,b), but also naturally leads to a range in final (^{231}Pa/^{235}U) and (^{230}Th/^{238}U) ratios that are more restricted than observed. Conversely, the larger range in (^{231}Pa/^{235}U) and (^{230}Th/^{238}U) ratios in the flux melting models stems from a very big range in total extent of melting (1–15%) which seems unrealistic considering the tholeiitic to calc-alkaline nature of the majority of rocks analysed and given that

Table 2
Source mode and partition coefficients used in numerical models[a]

Phase	Fertile mode	Depleted mode[b]	U	Th	Pa	Ra	Ba	Nb	La	Tb	Yb
Olivine	52	65	6.0E−05	9.5E−06	6.0E−08	5.8E−08	5.0E−06	5.0E−05	2.0E−04	1.5E−03	2.4E−02
Orthopyroxene	28	35	7.8E−03	3.0E−03	7.8E−06	6.0E−07	6.0E−06	3.0E−04	3.1E−03	1.9E−02	3.8E−02
Clinopyroxene	18	0	1.8E−02	2.1E−02	1.8E−09	4.1E−06	3.0E−04	8.9E−03	8.9E−02	1.1E+00	1.4E+00
Garnet	2	0	1.7E−02	3.3E−03	5.8E−04	7.0E−09	7.0E−05	3.5E−03	1.0E−02	7.5E−01	4.0E+00

[a] Based on Blundy and Wood (2003), Blundy et al. (1998) and the compilation of Halliday et al. (1995).
[b] Used for Tonga models only.

Table 3
Parameters employed in ageing + dynamic melting and flux melting calculations shown in Figs. 6, 11–18 (partition coefficients as in Table 2)

	Fig. 6	Tonga	Kermadec	Lesser Antilles	Vanuatu	Sunda	Mariana	Kamchatka	Alaska-Aleutians
Physical parameters									
Melt fraction in ageing + dynamic models (X)	0.1	0.1	0.1	0.1	0.1	0.1	0.1	0.1	0.1
F step in flux melting models (%)	0.0001	0.0001	0.0001	0.0001	0.0001	0.0001	0.0001	0.0001	0.0001
Residual porosity (ϕ)	0.002	0.002	0.002	0.002	0.001	0.002	0.002	0.001	0.001
Melt density ($\rho_{m'}$, kg/m^3)	2800	2800	2800	2800	2800	2800	2800	2800	2800
Solid density ($\rho_{s'}$, kg/m^3)	3300	3300	3300	3300	3300	3300	3300	3300	3300
Subduction rate (=W, cm/yr)[a]	2.4	17	7	2.4	11	6.7	4.8	9	6.2
Dip(θ)[a]	22	28	30	22	44	21	24	25	50
Melting rate (M, kg/m^3/yr)	1.32E−04	7.01E−04	4.60E−04	1.98E−04	7.26E−04	5.53E−04	3.17E−04	5.94E−04	4.09E−04
Melt region length, km (ageing + dynamic)	60	80	50	40	50	40	50	50	50
Melt region down dip length, km (flux melting)	180	240	150	120	150	120	150	150	150
Mantle composition prior to fluid addition[b]									
U (ppm)	0.015	0.006	0.01	0.015	0.015	0.015	0.015	0.015	0.015
Th (ppm)	0.046	0.017	0.031	0.046	0.046	0.046	0.046	0.046	0.046
Ba (ppm)	1.2	5	5	1.2	2	1.2	10	10	7
Nb (ppm)	0.15	0.05	0.1	0.15	0.1	0.14	0.12	0.2	0.15
Fluid composition per increment in aging + dynamic ageing models									
U (ppm)	0.005	0.008	0.015	0.015	0.03	0.015	0.04	0.02	0.03
Ba (ppm)	2	4	7	2	5	2	7	12	8
(^{226}Ra/^{230}Th)	2	2	2	2	2	2	2	2	2
Duration of ageing after U addition (kyr)[c]	40	50	50	90	60	90	30	150	10
Fluid composition per increment in flux melting models									
dU/dF (ppm)	0.025	0.04	0.075	0.075	0.06	0.075	0.2	0.1	0.15
Fluid Ba/U	300	300	300	300	300	300	300	300	300
Fluid Ra/U	30	30	30	30	30	30	30	30	30

[a] Based on values given in Jarrard (1986) and Plank and Langmuir (1998).
[b] Source (peridotite + sediment) is assumed to be in secular equilibrium prior to fluid addition of U, Ba, and Ra.
[c] Used in ageing + dynamic melting models only and based on U–Th equiline age interpretations in references cited in Table 1.

much of the variation in La/Yb in Fig. 4A is likely to reflect the opposing effects of sediment (melt) addition and prior melt depletion. Another important control on the extent of ^{231}Pa in-growth and final (^{231}Pa/^{235}U) ratios is the dimension of the melting region which will always be bigger in the flux melting model compared with that the dynamic melting model for a given (^{231}Pa/^{235}U) ratio. For the models shown in Figs. 11–18 the down-dip dimension of the melting region in the flux melting model is three times longer than that used in the dynamic models and Bourdon et al. (2003a,b) have questioned whether melts formed across such a large region can be efficiently focussed to the line of arc front volcanoes.

There has also been considerable recent discussion as to whether Th and Pa may have enough mobility in subduction zone fluids to influence U–Th–Pa disequilibria (e.g., Bourdon et al., 2003a,b; Sigmarsson et al., personal communication; Thomas et al., 2002). The grey curves in Figs. 13–18 show that simulating the steeper trends in the Nb-normalised diagrams would require a (^{231}Pa/^{235}U) ratio of 2 in the fluid in the flux melting models which seems extremely implausible given the insolubility of Pa relative to U. Moreover, although the presence of Pa in the fluid might help explain possible inverse correlations between (^{231}Pa/^{235}U) and (^{230}Th/^{238}U) in the Sunda and Central Kamchatka Depression (see Figs. 14A and B, and 15A and B), the existence of the former trend relies heavily on the Iya sample which may be anomalous (cf. Section 3) and the latter has been explained by mixing with eclogitic slab melts (Dosseto et al., 2003). The southern Lesser Antilles data might be simulated with Pa in the fluid but adopting such a model would significantly overestimate the (^{231}Pa/^{235}U) ratios of the northern Antilles lavas and produce the wrong slope in the (^{231}Pa/^{235}U) versus Ba/Th diagram (see Figs. 13A and B). Moreover, the results of the flux melting model containing Pa in the fluid are demonstrably inapplicable to the (^{231}Pa/^{235}U) versus (^{230}Th/^{238}U) and (^{231}Pa/^{235}U) versus Ba/Th trends observed in the Vanuatu, Mariana, and Alaska-Aleutian arcs (Figs. 14A and B, 16A and B, and 18A and B). Thus, until experimental or theoretical data indicate otherwise we remain sceptical that subduction zone fluids carry sufficient Pa (or Th) to significantly affect ^{231}Pa–^{235}U (or ^{230}Th–^{238}U) disequilibria and appeal below to intra-wedge mixing effects to explain some of the apparently anomalous data.

Thomas et al. (2002) utilised a plot of (^{231}Pa/^{230}Th) versus (^{238}U/^{230}Th) to illustrate their flux melting model. In this diagram mixing is linear, fluid addition is horizontal to the right, and the effects of ageing and in-growth curve upward to the left (see Thomas et al., 2002). We plot the global dataset in such a diagram in Fig. 8 which shows that most arcs other than Tonga form relatively steep trends. Representative numerical models show that overall the flux melting models produce shallower trends than the dynamic + ageing models. The shallow Tonga trend can reasonably be reproduced by either model but the steeper trends

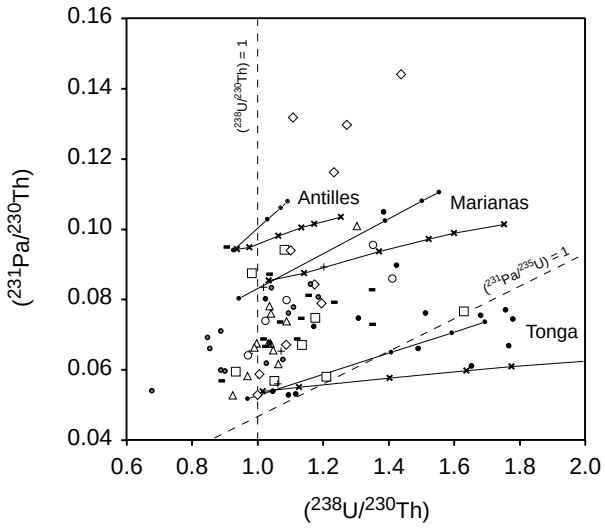

Fig. 8. Plot of (^{231}Pa/^{230}Th) versus (^{238}U/^{230}Th). Also plotted are dynamic + ageing (dotted trend) and flux melting (trend with crosses) models for three representative arcs suiting the parameters given in Tables 2 and 3. Data sources and symbols as in Fig. 2.

from many of the other arcs are perhaps better simulated by dynamic melting + ageing. However, whereas the slope can be approximated by the latter models, the range of data cannot and this again emphasises that along-arc source variations, which allow for a greater relative fractionation of U/Th ratios, must be important.

We have not focussed on the ^{226}Ra–^{230}Th system because the timing of addition of the final fluid contributions (which are inferred to be largely responsible for observed ^{226}Ra excesses) and partial melting are likely to overlap. Furthermore, there is good evidence for a decrease in (^{226}Ra/^{230}Th) with increasing SiO_2 in a number of arcs, suggesting that the primary ^{226}Ra–^{230}Th signature may often be modified by decay during differentiation in the crust (e.g., Turner et al., 2001). Nevertheless, both the ageing + dynamic melting and flux melting models can produce primary (^{226}Ra/^{230}Th) ratios >4 and predict a negative correlation between (^{226}Ra/^{230}Th) and (^{231}Pa/^{235}U) as broadly observed in the global dataset (see Fig. 3A).

7. A role for mixing

Much of the preceding discussion highlights that there is no single model which can replicate all of the data trends and in a number of instances the data lie at a high angle to those predicted by any of the models (e.g., Figs. 13A and B, 14B, and 18B). This is somewhat reminiscent of the global and local vectors in the $Fe_{8.0}$–$Na_{8.0}$ systematics of MORB, the latter being attributed to mixing between small melt fractions formed deep in the melting column with larger degree melts produced higher up (Brodholt and Batiza, 1989; Klein and Langmuir, 1989). In subduction zones, $Fe_{8.0}$–$Na_{8.0}$ systematics can be strongly influenced by the effects of depletion due to prior melt

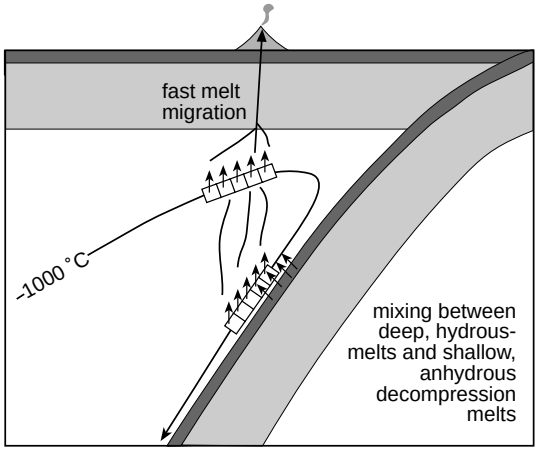

Fig. 9. Illustration of one possible model in which deep, hydrous melts produced by either of the mechanisms in Fig. 5B or C are mixed with shallower, anhydrous melts produced by decompression in the upwelling limb of the wedge convection system (cf. Fig. 5A).

extraction in the back-arc environment (e.g., Taylor and Martinez, 2003; Turner et al., 1997). By analogy with the MORB models, we now explore likely intra-wedge effects on ^{231}Pa–^{235}U isotopes by investigating mixing between a small degree dynamic melt formed at depth with a larger degree melt formed more shallowly and over a larger melt column. In practice, in the arc environment this model may reflect mixing of deeper, hydrous melts produced just above the slab (cf. Figs. 5B or C) with hotter, dryer melts (e.g., Elkins Tanton et al., 2001; Sisson and Bronto, 1998) produced at shallower depths by decompression in the upwelling limb of induced convection (cf. Fig. 5A; Conder et al., 2002) as illustrated in Fig. 9. Indeed, the high (^{230}Th/^{238}U) end of the global array in Fig. 2A is tied to samples with ^{230}Th excesses that, from a U-series perspective, look like conventional decompression melts of anhydrous peridotite (i.e., MORB; see Fig. 2A) and addition of these may be required in order to achieve an integrated 15% melting in light of the low melt productivity of hydrous peridotite (Gaetani and Grove, 1998; Hirschmann et al., 1999).

Melt productivity from hydrous peridotite at the onset of melting is lower than for anhydrous peridotite even though melting initiates at a lower temperature (Gaetani and Grove, 1998; Hirschmann et al., 1999). The combination of fluid addition, and low rates and degrees of melting results in greater extents of ^{231}Pa–^{235}U disequilibria in the model deep melts relative to the shallow ones and might explain why the Iya and Matthew samples have so much higher (^{231}Pa/^{235}U) ratios than those of other samples from the same arcs. In Fig. 10 we illustrate how intra-wedge mixing can also lead to negative trends between (^{231}Pa/^{235}U) and (^{230}Th/^{238}U) coupled with positive trends between (^{231}Pa/^{235}U) and Ba/Th. This provides a potential explanation for the northern Antilles and Sunda data, and perhaps the positive (^{231}Pa/^{235}U) versus Ba/Th correlations in the Vanuatu and Alaska-Aleutian arcs. An important corollary is that the effects of mixing may remove any *necessity*

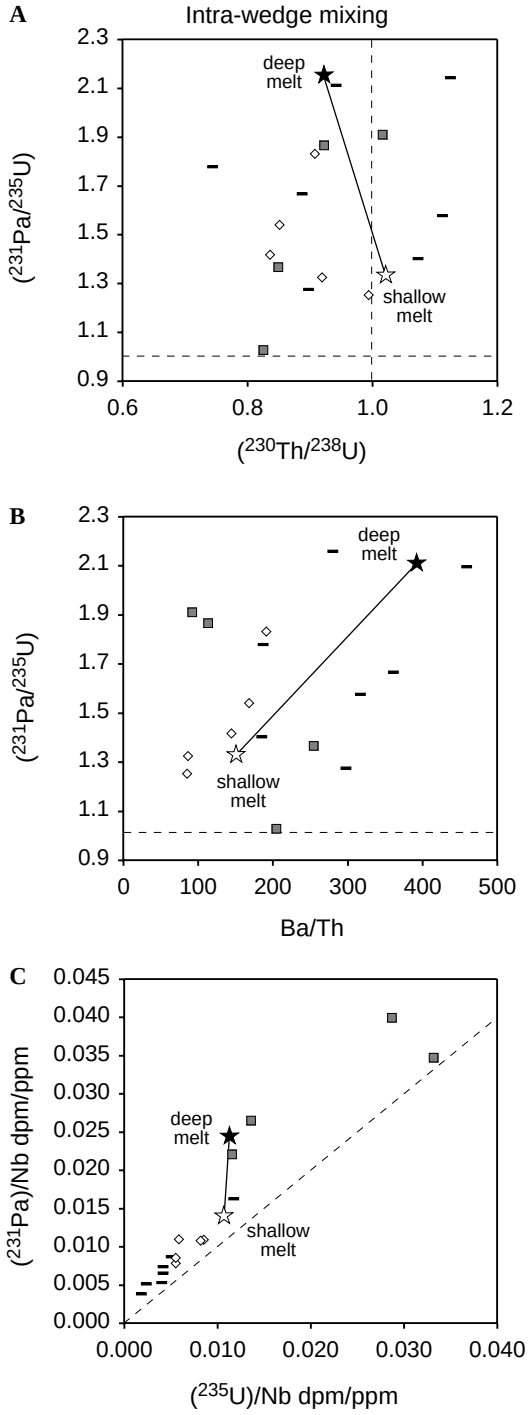

Fig. 10. Plots of (A) (^{231}Pa/^{235}U) versus (^{230}Th/^{238}U), (B) (^{231}Pa/^{235}U) versus Ba/Th, and (C) (^{231}Pa)/Nb versus (^{235}U)/Nb showing the effects of mixing. The deep melt is a hydrous (i.e., U-enriched) 1% dynamic melt formed at 1.98×10^{-4} kg/m^3/yr between 100 and 90 km depth in the presence of 2% residual garnet whereas the shallow melt is an anhydrous (i.e., the source was assumed to be in secular equilibrium) 20% dynamic melt formed at 7.92×10^{-4} kg/m^3/yr between 90 and 50 km depth in the absence of residual garnet. The deeper, fluid-enriched source had 0.02 ppm U, 0.046 ppm Th, 16 ppm Ba, and 0.05 ppm Nb, whereas the shallower, dryer source had 0.015 ppm U, 0.046 ppm Th, 8 ppm Ba, and 0.05 ppm Nb. The residual porosity was 0.002 and the subduction rate 6 cm/yr; all other parameters as for Fig. 6 and in Table 2. Superimposed are data from the northern Lesser Antilles, Vanuatu away from the D'Entrecasteaux collision zone and continental Alaska.

in our data to mobilise Pa (or Th) in the fluid phase. Interestingly, mixing effects also lead to a steep vector on the Nb-normalised diagram (Fig. 10C) and so this may also explain why the data from some arcs, such as Sunda, are quite scattered in this diagram (see Fig. 15C) whereas others, exemplified by the Marianas (Fig. 16C), form well-correlated linear arrays. Lastly, the effect of mixing is also to produce a negative correlation between (^{226}Ra/^{230}Th) and (^{231}Pa/^{235}U) as broadly observed in Fig. 3B. Unfortunately, possible ^{226}Ra decay during differentiation makes this prediction hard to test without an expanded suite of very primitive lavas.

8. Concluding remarks and summary

We have presented new ^{231}Pa data for 50 well-characterised lavas from seven different arcs to significantly expand the published database. The original intention of this work was to investigate potential global systematics, such as those broadly found for the ^{230}Th–^{238}U and ^{226}Ra–^{230}Th systems. Although no such simple picture has emerged, broad positive correlations between (^{231}Pa/^{235}U) and (^{230}Th/^{238}U) and La/Yb, and much weaker negative tends between (^{231}Pa/^{235}U), and both Ba/Th and (^{226}Ra/^{230}Th) suggest that (^{231}Pa/^{235}U) tends to be higher in sediment-rich arc lavas because the effects of fluid addition are muted and so there is less of a deficit of ^{231}Pa for the melting effect to overprint. It appears that either ageing + dynamic melting or flux melting can explain the *range* of (^{231}Pa–^{235}U) ratios in arc lavas without recourse to invoking Pa or Th in the fluid (but see also Thomas et al., 2002). However, data from individual arcs are often scattered. Consequently, it is not easy to discriminate between these two models which in essence do very similar things because the progressive incremental fluid addition in the flux models leads to ageing of the average integrated time of fluid U addition (Thomas et al., 2002). It appears that variable source composition, degree of melting, and the effects of mixing of magmas generated at different depths and under different conditions in the mantle wedge must be important in some segments of several different arcs.

In summary, the new Pa–U data, together with the results of previous Th–U and Ra–Th studies of arc lavas, show that:

- (^{230}Th/^{238}U) ratios are typically <1 reflecting fluid U addition from the slab; debate continues as to whether the inclined arrays on the U–Th equiline diagram reflect the integrated time since fluid U addition (but see discussions by Bourdon et al., 2003a,b and Turner et al., 2003), the effects of partial melting (e.g., George et al., 2003) or the presence of some Th in the fluid (e.g., Thomas et al., 2002).
- (^{231}Pa/^{235}U) ratios are almost ubiquitously >1 (cf. Pickett and Murrell, 1997) requiring that the effects of partial melting overprint those of sediment (melt) and fluid addition.
- The magnitude of the (^{231}Pa/^{235}U) ratios requires in-growth melting models in which the peridotite matrix moves through the melting region, remaining above its solidus, for ~1 Myr and ^{231}Pa–^{235}U disequilibria are sensitive to anything which affects that. The movement of the peridotite matrix may be due to decompression or, because it is coupled to the subducting slab and consequently dragged down through the zone of melt generation. The models presented in Figs. 6, 7, and, 12–18 are certainly permissive of the hypothesis that the matrix movement is linked to convection in the mantle wedge and the rate of subduction.
- Overall there is a positive correlation between (^{231}Pa/^{235}U) and (^{230}Th/^{238}U) (Fig. 2A). The samples lie on an array broadly parallel to the U addition vector which results from the combined effects of fluid addition and in-growth melting, rather than reflecting the clinopyroxene/garnet ratio during melting as is inferred for MORB and OIB (Bourdon and Sims, 2003).
- Variations in critical parameters (e.g., source composition and extent of melting) both between different subduction zones and even within individual subduction zones exert a major influence in controlling variations in ^{231}Pa–^{235}U disequilibria in arc lavas.
- Mixing effects may be important in a number of arc segments and highlight that each dataset should be evaluated individually. Mixing may occur between shallower, high temperature, drier decompression melts and deeper, lower temperature, and wetter melts formed just above the subducting plate.
- Melt segregation and ascent is constrained by (^{226}Ra/^{230}Th) > 1 and (^{228}Ra/^{232}Th) = 1 (Turner et al., 2004) to occur in less than a few 1000 but more than 30 years implying rapid transport of melts and therefore minimal chromatographic melt–wall rock interaction; the formation of some ^{226}Ra–^{230}Th disequilibria via steady-state diffusion in the source (Feineman and DePaolo, 2000) does not relax this constraint (George et al., 2004).

Acknowledgments

The sample set on which this work is based was provided through the generosity of Irwan Bahar, Sutikno Bronto, Tony Crawford, Marc Defant, Steve Eggins, Tony Ewart, John Foden, Rhiannon George, Jim Gill, Bob Kay, Pavel Kepezhinskas, Ray Macdonald, Chris Nye, Lin Sutherland, Tracy Vallier, Steve Weaver, Jon Woodhead, and Georg Zellmer. We especially thank Marc Hirschmann for providing a copy of the flux melting spreadsheet and Jim Gill, Bernard Bourdon, and Dave Peate for their detailed and very helpful reviews. Many helpful discussions were held with Bernard Bourdon, Tim Elliott, and Mark Reagan. Thanks to Julie Prytulak for advice on calculating activity ratios. This work was funded by the NERC (GR3/13171), the Leverhulme

Trust (F/00182/H), and a Royal Society Small Research Grant whilst S.T. was supported by a Royal Society University Research Fellowship and subsequently an Australian Federation Fellowship.

Associate editor: Martin A. Menzies

Appendix A. Variations within subduction zones

A.1. Tonga

We start by briefly reviewing Tonga because this arc forms an end-member due to its highly depleted nature and the preservation of ^{231}Pa deficits (Bourdon et al., 1999; Turner et al., 1997, 2000). Plotted in Fig. 11 are the data from Bourdon et al. (1999) combined with the new analyses presented in Table 1 showing that half have ^{231}Pa deficits. Overall the data form a positive array in the plot of (^{231}Pa/^{235}U) versus (^{230}Th/^{238}U) in Fig. 8A with two of the new analyses (Tafahi and 'Ata) at quite high (^{231}Pa/^{235}U). In the (^{231}Pa/^{235}U) versus Ba/Th diagram the data form a scattered negative array if the Tafahi and 'Ata samples are included.

The original finding of Bourdon et al. (1999) was that many of the Tonga lavas (and one Kermadec lava) form a line on the Nb-normalised isochron diagram which corresponds to 60 kyr similar to the 50 kyr line through the same data in a U–Th equiline diagram (Turner et al., 1997). Fig. 11C shows that, including the new data, four samples lie above these lowermost data. Bourdon et al. (1999) inferred that the Tonga samples had not had their ^{231}Pa–^{235}U systematics significantly affected by partial melting due to a lack of residual clinopyroxene. However, our modelling shows that even a source composed only of olivine and orthopyroxene will lead to an increase in (^{231}Pa/^{235}U) during melting, although neither dynamic melting without ageing nor flux melting can easily simulate the data (see Fig. 11C). In Fig. 11C we show the effects of dynamic melting of a clinopyroxene- (and garnet-) free source which had undergone fluid U addition 50 kyr earlier and this bisects the data suggesting that the simplest explanation for the four samples with higher (^{231}Pa/^{235}U) ratios is that they contain the greatest melting effect. Returning to Figs. 11A and B it can be argued that the same dynamic + ageing model best replicates the systematics of the Tonga data in these diagrams.

A.2. Kermadec

The Kermadec data are plotted in Fig. 12 forming a more scattered (^{231}Pa/^{235}U) versus (^{230}Th/^{238}U) array and a steep (^{231}Pa/^{235}U) versus Ba/Th array (Figs. 12A and B). One sample has a ^{231}Pa deficit and also lies on the 60 kyr line in Fig. 12C. For our modelling of the Kermadec data we have assumed a slower convergence and matrix flowrate, and a more fertile source and source mineralogy (Tables 2 and 3). Interestingly, it is the dynamic melting without ageing and flux melting models which most closely replicates the slopes of the arrays formed by the data in Figs. 12A and B. However, the two samples with highest (^{231}Pa/^{235}U) would appear to be more consistent with 50 kyr of ageing between fluid U addition and partial melt-

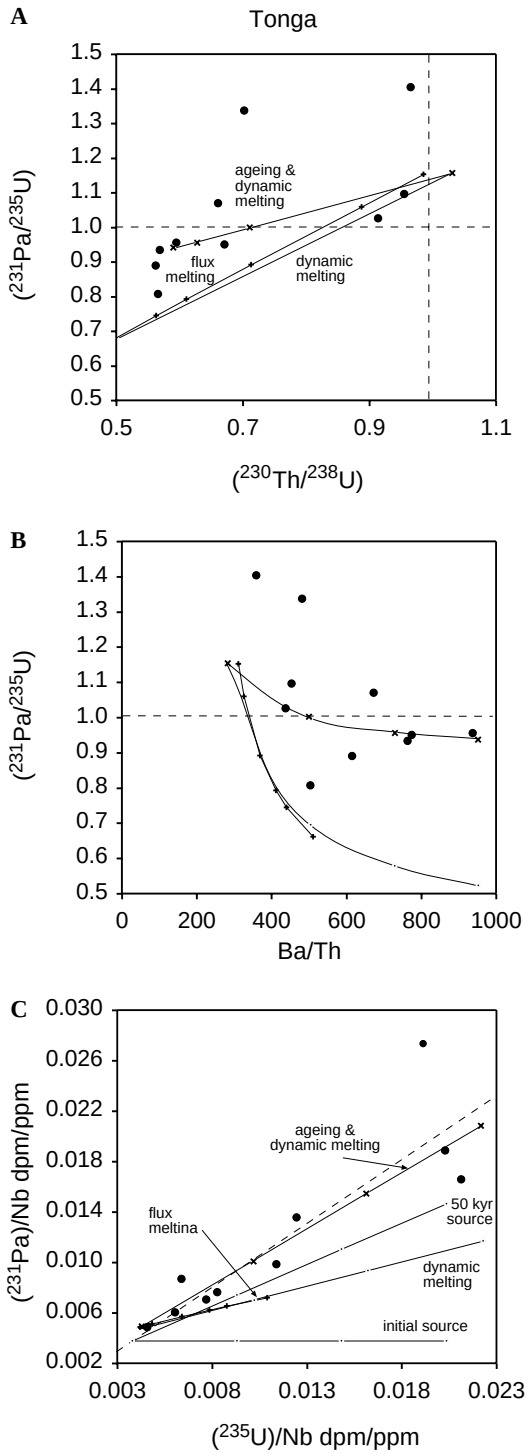

Fig. 11. Plots of (A) (^{231}Pa/^{235}U) versus (^{230}Th/^{238}U), (B) (^{231}Pa/^{235}U) versus Ba/Th, and (C) (^{231}Pa)/Nb versus (^{235}U)/Nb for Tonga along with various melting models as illustrated in Fig. 7 (input parameters are given in Tables 2 and 3). Data from Table 1 and Bourdon et al. (1999).

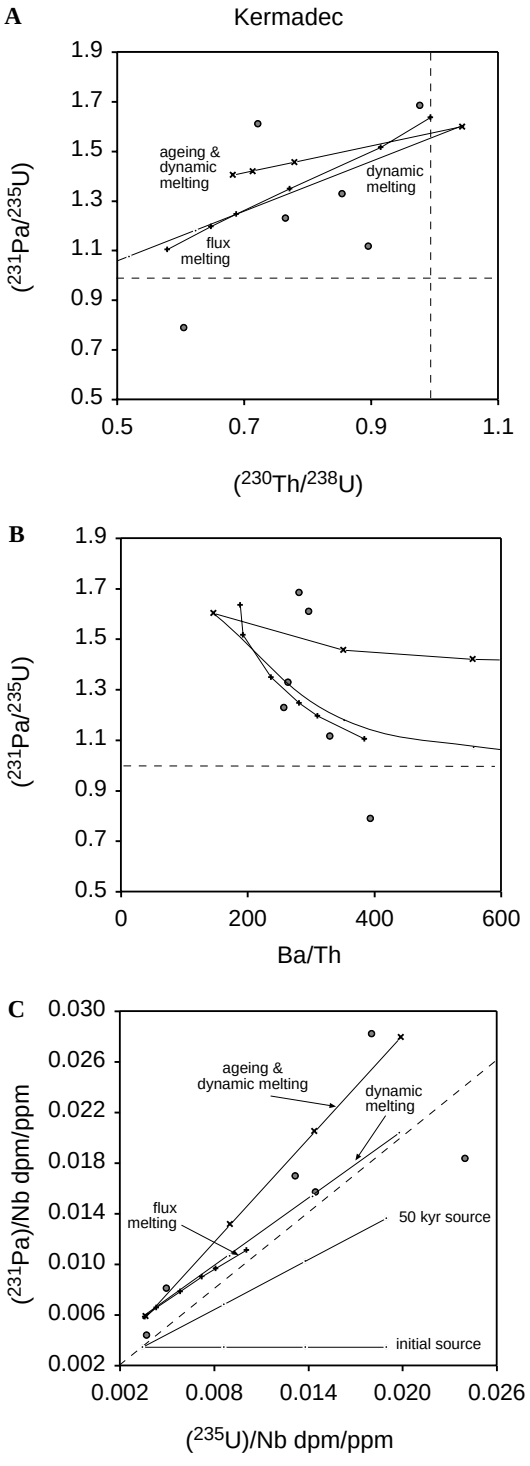

Fig. 12. Plots of (A) (^{231}Pa/^{235}U) versus (^{230}Th/^{238}U), (B) (^{231}Pa/^{235}U) versus Ba/Th, and (C) (^{231}Pa)/Nb versus (^{235}U)/Nb for Kermadec along with various melting models as illustrated in Fig. 7 (input parameters are given in Tables 2 and 3). Data from Table 1 and Bourdon et al. (1999).

ing. In Fig. 12C, four of the five samples with ^{231}Pa excesses lie close to the dynamic + ageing model curve.

In summary, some melting effects are discernible in the Tonga–Kermadec ^{231}Pa–^{235}U data. With the exception of the Tafahi sample, (^{231}Pa/^{235}U) generally increases southwards along the arc and we infer that this reflects an increasing proportion of residual clinopyroxenes during melting. However, if the fast subduction rate in Tonga corresponds to a fast matrix flow rate, then this will also act to diminish the effects of melting on U-series disequilibria (cf. Fig. 7). As we will see below, the lack of consistent adherence of the data to any one of the three melting models being tested is a repetitive feature of the arc datasets and may say as much about the similarities of the models as anything else.

A.3. Lesser Antilles

The Lesser Antilles arc has a very slow subduction rate and the eruptive products broadly change from tholeiitic to calc-alkaline to increasingly alkalic southwards along the arc (Macdonald et al., 2000). This affords the opportunity to investigate variations in ^{231}Pa–^{235}U disequilibria with bulk rock composition and magmatic affinity which may, in part, be linked to changing depth and degrees of partial melting. The ^{231}Pa data are plotted in Fig. 13, subdivided into samples from the northern and southern parts of the arc which highlights the significantly higher (^{231}Pa/^{235}U) ratios in the majority of the southern lavas. The exception is a sample from Grenada but the age of this sample is poorly constrained and so an unknown amount of decay may have occurred since eruption. Nevertheless, the difference between north and south in the arc could, in the dynamic melting models, reflect significantly lower average degrees of melting in the south. The oceanic plate also subducts more obliquely at a shallower dip in the south which might lead to lower wedge temperatures and slower melting rates (cf. Bourdon et al., 2003a,b) which would also serve to increase (^{231}Pa/^{235}U) ratios. Interestingly, whilst several authors have invoked a significant role for residual garnet in the southern Antilles (e.g., Shimizu and Arculus, 1975), this should produce lower (^{231}Pa/^{235}U) and higher La/Yb, both of which are the opposite of what is actually observed (Figs. 4C and 13A).

On the (^{231}Pa/^{235}U) versus (^{230}Th/^{238}U) plot in Fig. 13A, the Antilles lavas broadly form a negative array, especially the northern lavas, and the northern and southern samples (excepting Grenada) form divergent trends in Fig. 13B. The Nb-normalised plot in Fig. 13C shows that the Antilles lavas form a very steep array above the "equiline." Whilst mixing can produce straight arrays on this diagram, simple two-end-member mixing is ruled out by the divergent arrays in Fig. 13B. Using the parameters in Tables 2 and 3, the dynamic, ageing + dynamic melting, and the flux melting models can all reproduce the average compositions of the southern lavas in Fig. 13 but none is able to reproduce the negative trend of the northern Antilles lavas in Fig. 13A or their positive trend in Fig. 13B. In the Nb-normalised diagram, the ageing + dynamic melting model produces a steeper trend than the flux melting model because the 90 kyr of ageing subsequent to fluid U addition (cf. Turner et al., 1996) results in the wedge compositions lying along a relatively steep array before the effects of partial melting are superimposed. However, the combined data array is steeper than that of any of the models.

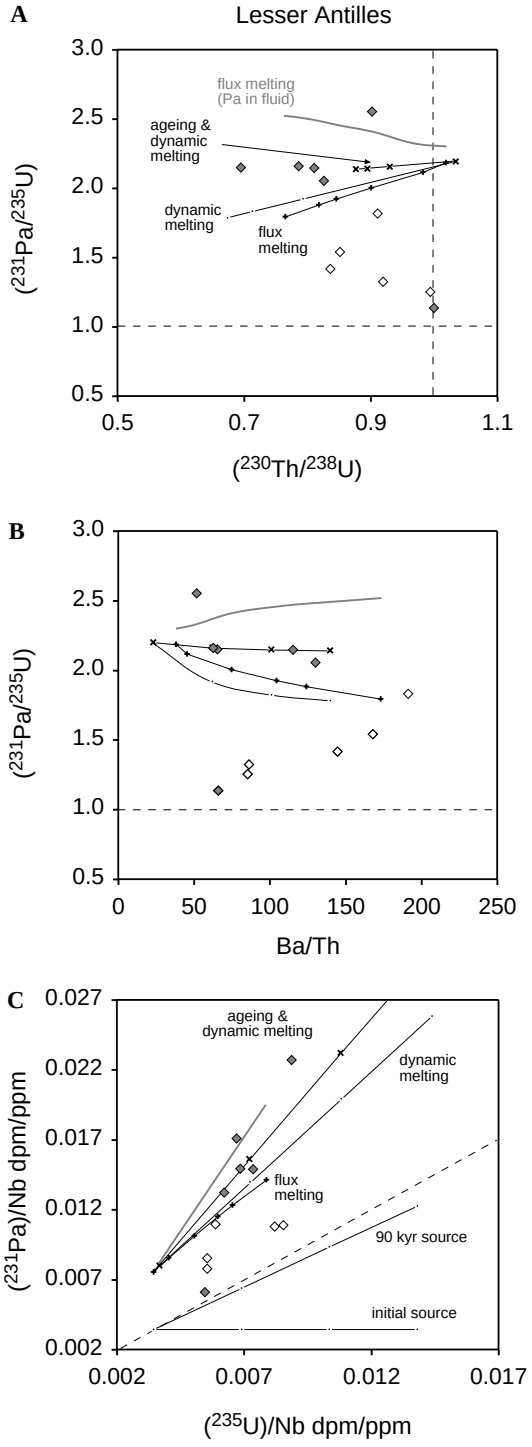

Fig. 13. Plots of (A) (^{231}Pa/^{235}U) versus (^{230}Th/^{238}U), (B) (^{231}Pa/^{235}U) versus Ba/Th, and (C) (^{231}Pa)/Nb versus (^{235}U)/Nb for the Lesser Antilles along with various melting models as illustrated in Fig. 7 (input parameters are given in Tables 2 and 3). Shaded symbols are data from the southern islands, St. Vincent to Grenada, including the data for Kick 'em Jenny. Data from Table 1 and Pickett and Murrell (1997).

A.4. Vanuatu

Some of the interesting features of the Vanutau arc include the tendency for the erupted products to be very primitive and often picritic (e.g., Eggins, 1993), and the collision with the D'Entrecasteaux Ridge which results in a decrease in subduction rate in this locality (Taylor et al., 1995). This region is also characterised by a change from Pacific- to Indian-type mantle composition (Crawford et al., 1995). Turner et al. (1999) found that the U–Th isotope systematics differed across these regions and that there was an inferred decrease in the integrated timing of fluid U addition in the zone of collision. Nevertheless, from Fig. 14 it appears that there is no simple distinction in the ^{231}Pa systematics between the samples taken from the collision zone and those outside its influence.

In contrast to the Lesser Antilles, (^{231}Pa/^{235}U) is broadly positively correlated with (^{230}Th/^{238}U) in Fig. 14A although the two samples from the southernmost island of Matthew are displaced to higher (^{231}Pa/^{235}U). The Matthew samples have high Zr/Y (and Sr/Y) compared with the rest of the Vanuatu samples which along with their high (^{231}Pa/^{235}U) may reflect lower average degrees of melting in a cooler corner portion of the arc. The dynamic, ageing + dynamic melting, and the flux melting models can produce positive trends which pass through the majority of data in this diagram excepting the Matthew samples in Fig. 14A. In the plot of (^{231}Pa/^{235}U) versus Ba/Th (Fig. 14B) six of the samples seem to form a positive array although the displacement of the two Matthew samples to higher (^{231}Pa/^{235}U) and lower Ba/Th is consistent with the broad negative correlation in the global dataset in Fig. 3A. As noted above, both the dynamic melting and the flux melting models produce negative trends in Fig. 14B which pass below any of the data. The ageing + dynamic melting model yields higher (^{231}Pa/^{235}U) ratios and can pass through the data, albeit without reproducing the apparent positive trend in the data. Finally, in the Nb-normalised diagram (Fig. 14C), neither the dynamic nor flux melting models can produce trends with slopes as steep as the data. In contrast, the ageing + dynamic melting model can produce a trend which passes through the centre of the scattered data if the time since fluid U addition is ~60 kyr. This is consistent with the apparent U–Th isochron through the non-collision zone lavas (Turner et al., 1999) but ageing for only 16 kyr, as inferred for those volcanoes away from the D'Entrecasteaux collision zone (Turner et al., 1999), does not allow sufficiently steep trends to be reproduced in Fig. 14C without reducing either the extent of melting or residual porosity or increasing the length of the melting column. Matthew lies off all single source models.

A.5. Sunda

The Sunda samples come from the arc segment which is built upon oceanic crust between Java and the site of the Australian collision to the east of Flores (Hamilton, 1979). The arc front samples include a close to primary composition basalt from Galunggung in Java (Gerbe et al., 1992), which has a (^{231}Pa/^{235}U) ratio of 1.6. This may be contrasted with the arc front sample from Iya in

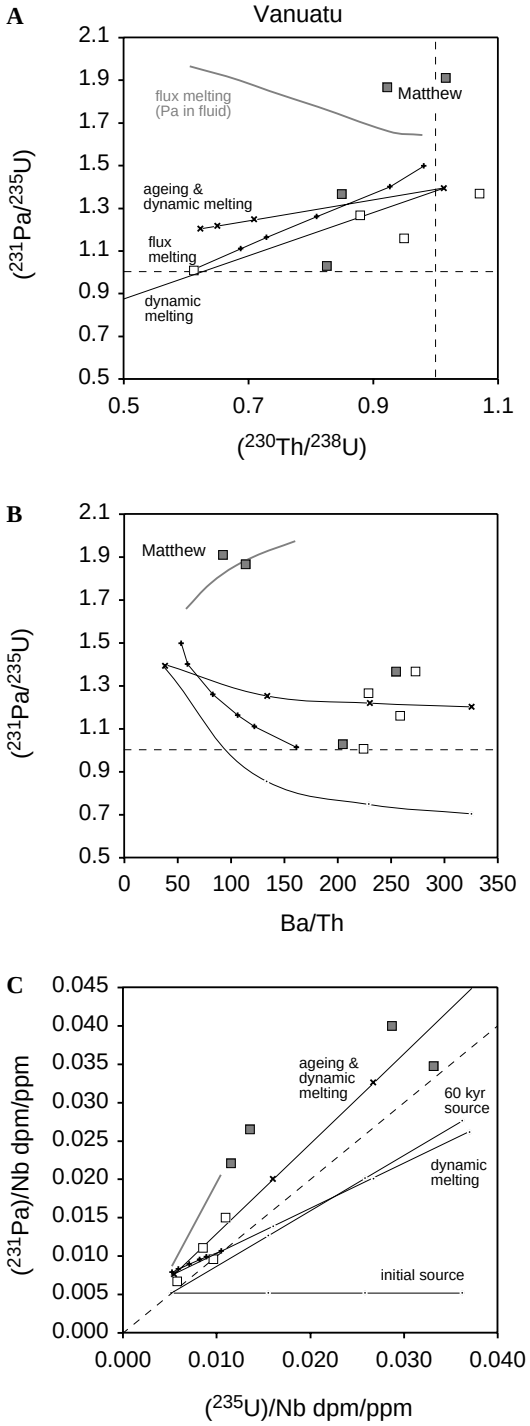

Fig. 14. Plots of (A) (^{231}Pa/^{235}U) versus (^{230}Th/^{238}U), (B) (^{231}Pa/^{235}U) versus Ba/Th, and (C) (^{231}Pa)/Nb versus (^{235}U)/Nb for Vanuatu along with melting models as illustrated in Fig. 7 (input parameters are given in Tables 2 and 3). Shaded symbols are data from the southern islands whereas the open symbols are islands in the D'Entrecasteaux Collision Zone. Data from Table 1.

Flores which has a much more pronounced fluid signal (Ba/Th = 217, (^{230}Th/^{238}U) = 0.55) but an even higher (^{231}Pa/^{235}U) ratio of 2.4 or from Rindjani which has a much lower (^{231}Pa/^{235}U) ratio of 1.1. This arc also provides the opportunity to investigate changes in melting signature with increasing depth to Benioff zone (e.g., Hutchison, 1976) because, on Sumbawa, the samples from Sangenang Api and Tambora lie significantly behind the arc front volcano of Rindjani. Interestingly, the (^{231}Pa/^{235}U) ratios from Sangenang Api and Tambora are significantly higher (1.3 and 1.8, respectively) than that from Rindjani (1.1) and this may reflect the lower extents of melting initiated at greater depths beneath these rear-arc volcanoes. However, Iya from nearby Flores on the arc front has a (^{231}Pa/^{235}U) ratio of 2.4.

In Fig. 15A, the Sunda data form a cluster on a plot of (^{231}Pa/^{235}U) versus (^{230}Th/^{238}U). As noted earlier, the Iya sample lies at much higher (^{231}Pa/^{235}U) than most arc front, low-K lavas having low (^{230}Th/^{238}U). This may hint at an overall negative correlation, as observed in the Lesser Antilles. However, the melting signature appears to be highly variable along the arc front and overall the data form a positive array in Fig. 15B which differs from the apparent anti-correlation hinted at in the global array in Fig. 3A. The ageing + dynamic melting and the flux melting models pass through the main cluster of data in Figs. 15A though the dynamic melting without ageing model produces (^{231}Pa/^{235}U) ratios which are too low at a given Ba/Th ratio in Fig. 15B. Because all these models produce negative tends in Fig. 15B, they cannot extend to the anomalous Iya data point. In Fig. 15C, the Sunda samples form rather scattered positive trends between (^{231}Pa)/Nb and (^{235}U)/Nb. These samples are also dispersed on the U–Th equiline diagram, with the Iya data suggesting very recent fluid U addition whereas most other samples have higher (^{230}Th/^{232}Th) possibly indicating a longer integrated time since fluid U addition (Turner and Foden, 2001). If Iya is excluded and we allow 90 kyr of ageing between fluid U addition and partial melting, the ageing + dynamic melting model can transect the data in Fig. 15C whereas the dynamic without ageing and flux melting models produce much shallower trends which do not pass close to the majority of data.

A.6. Marianas

The Mariana arc is entirely intra-oceanic with an extensive back-arc spreading system (Stolper and Newman, 1994) and the composition of the wedge and incoming sediments is apparently relatively constant (Elliott et al., 1997; Plank and Langmuir, 1998). This one of the simplest systems and has produced one of the more coherent geochemical datasets (Elliott et al., 1997). We present ^{231}Pa data on three samples which have been combined with two further samples analysed by Pickett and Murrell (1997) to allow a preliminary investigation of ^{231}Pa–^{235}U systematics in this arc but a far more comprehensive dataset (Elliott et al., 2001; Elliott, pers. comm.) is soon to be published. A noteworthy feature of the present dataset is that there is much less variation in (^{231}Pa/^{235}U) ratios (1.36–1.57) than that observed in any of the other arcs studied, suggesting that the partial melting process may be relatively uniform along

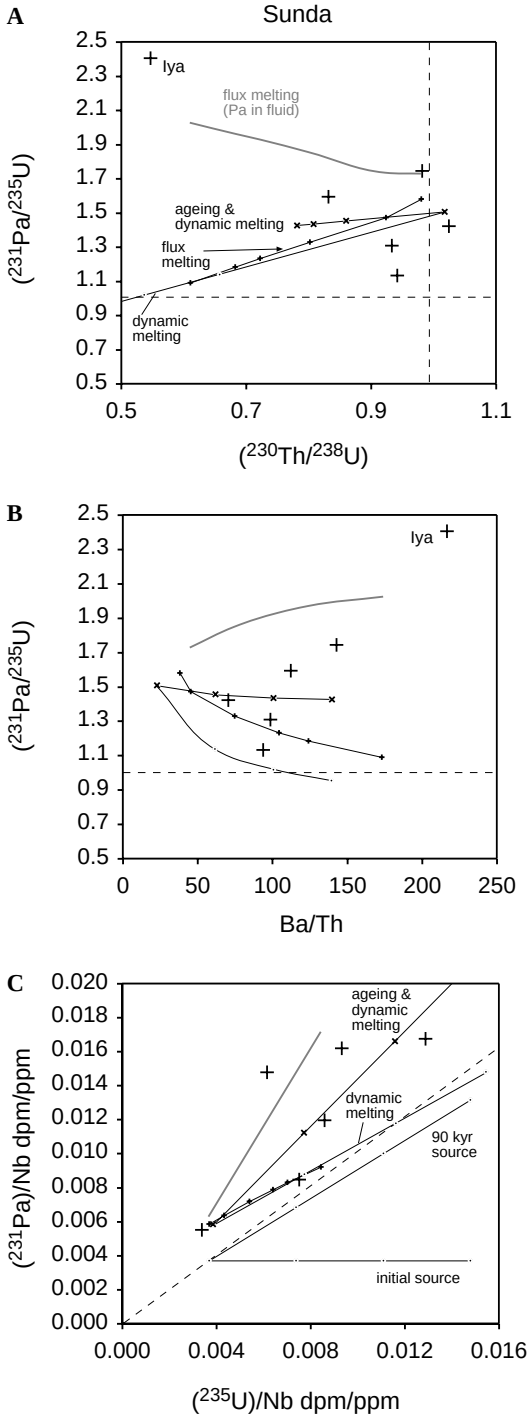

Fig. 15. Plots of (A) (^{231}Pa/^{235}U) versus (^{230}Th/^{238}U), (B) (^{231}Pa/^{235}U) versus Ba/Th, and (C) (^{231}Pa)/Nb versus (^{235}U)/Nb for the Sunda arc along with melting models as illustrated in Fig. 7 (input parameters are given in Tables 2 and 3). Data from Table 1 and Pickett and Murrell (1997).

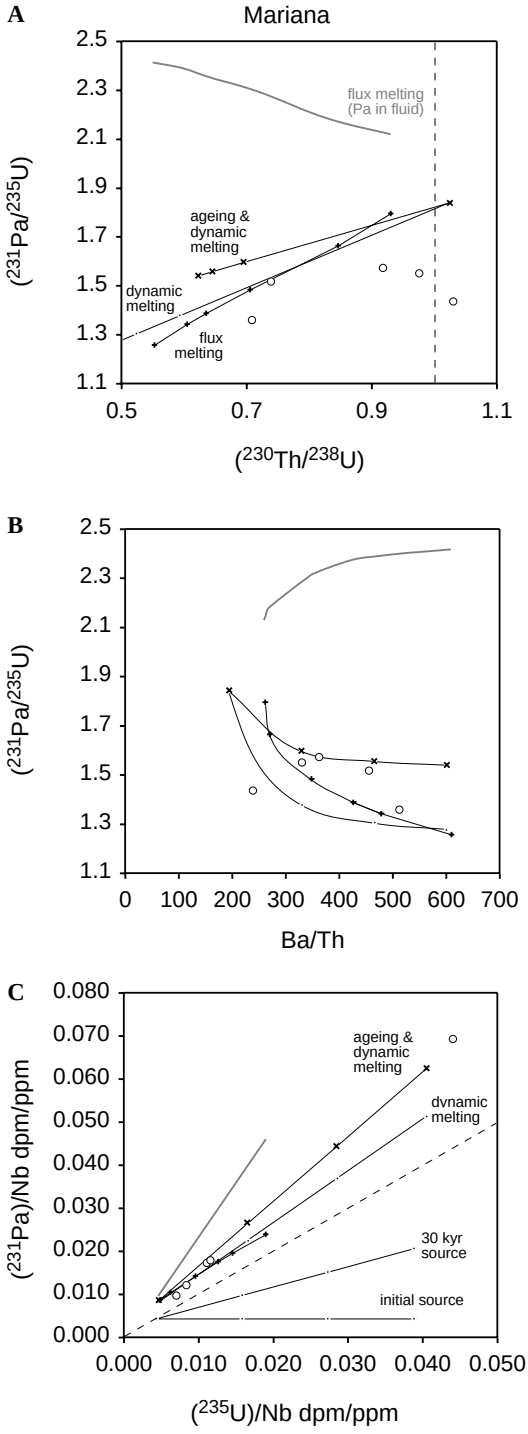

Fig. 16. Plots of (A) (^{231}Pa/^{235}U) versus (^{230}Th/^{238}U), (B) (^{231}Pa/^{235}U) versus Ba/Th, and (C) (^{231}Pa)/Nb versus (^{235}U)/Nb for the Marianas along with melting models as illustrated in Fig. 7 (input parameters are given in Tables 2 and 3). Data from Table 1 and Pickett and Murrell (1997).

the arc and that the effects of partial melting are less sensitive to the variations in the relative amounts of fluid addition inferred here.

Accordingly, the data form relatively horizontal arrays on the diagrams of (^{231}Pa/^{235}U) versus (^{230}Th/^{238}U) and (^{231}Pa/^{235}U) versus Ba/Th (Figs. 16A and B). In contrast, the dynamic melting, ageing + dynamic melting, and the flux melting models all produce positively sloped trends in Fig. 16A and whilst these can reproduce the average (^{231}Pa/^{235}U) and (^{230}Th/^{238}U) ratios, they form trends at a significant angle to the data. However, they do predict a trend of decreasing (^{231}Pa/^{235}U) with increasing Ba/Th

ratio which is similar to the global observation in Fig. 3A and can adequately replicate the observed data in Fig. 16B. On the Nb-normalised diagram (Fig. 16C), the data form a linear array ($R^2 = 0.9997$) and such arrays have been interpreted to have age significance (Bourdon et al., 1999). Interestingly, the dynamic melting and flux melting models underestimate the slope of this array, especially when the Pagan sample at high (^{235}U)/Nb, high (^{231}Pa)/Nb is considered. However, allowing the metasomatised wedge to age for 30 kyr subsequent to fluid U addition (Elliott et al., 1997) followed by dynamic melting produces a very good simulation of the data.

A.7. Kamchatka

The Kamchatka arc is of interest for several reasons. It is the only arc studied here that is built upon thick continental crust and there are two volcanic chains; the Eastern Volcanic Front (EVF) and the Central Kamchatka Depression (CKD) which lies behind the volcanic front in a zone of extension (Geist et al., 1994; Kepezhinskas et al., 1997). Therefore, this arc affords the opportunity to examine potential changes in melting regime with varying depth to the Benioff zone and crustal thickness. However, there is no clear separation of the EFV and CKD samples in ^{231}Pa–^{235}U systematics in Fig. 14A. The subducting slab is tearing beneath the northern part of the CKD giving rise to localised slab melts (so-called adakites) that are erupted at Sheveluch volcano in particular (Yogodzinsky et al., 2001). The high modal proportion of garnet in the slab compared to that of the mantle wedge should facilitate identification of slab melts and Dosseto et al. (2003) have inferred such components to have (^{230}Th/^{238}U) $\geqslant 1$ and (^{231}Pa/^{235}U) ~ 1 in a study of lavas from the Klyuchevskoy volcano group, which lies to the south of Sheveluch. Our silicic andesite sample from Sheveluch has the lowest (^{231}Pa/^{235}U) ratio of all of our samples from this arc but has a (^{230}Th/^{238}U) ratio of 0.94 and Sr/Y = 36.

In Fig. 17A, the Kamchatka samples form a cluster or possible negative (^{231}Pa/^{235}U)–(^{230}Th/^{238}U) array which cannot be simulated using any of the dynamic, ageing + dynamic melting or flux melting models. Dosseto et al. (2003) interpreted a similar array in their Klyuchevskoy suite in terms of mixing between slab and wedge melts but the U-excess of our Sheveluch sample does not seem to conform to this model easily. Interestingly, the CKD and EVF samples seem to form two positively sloped arrays on the (^{231}Pa/^{235}U) versus Ba/Th plot (Fig. 17B) whereas all of the numerical models yield negative trends. The steeper arrays formed by the dynamic without ageing or flux melting models can fit a mix of many of the CKD and EVF data, whereas the shallower ageing + dynamic melting model can fit the remainder. A key difference between the application of these models to this arc is that we have allowed for 150 kys of ageing after fluid U addition prior to melting (Turner et al., 1998) in the ageing + dynamic melting model. The consequence of this is

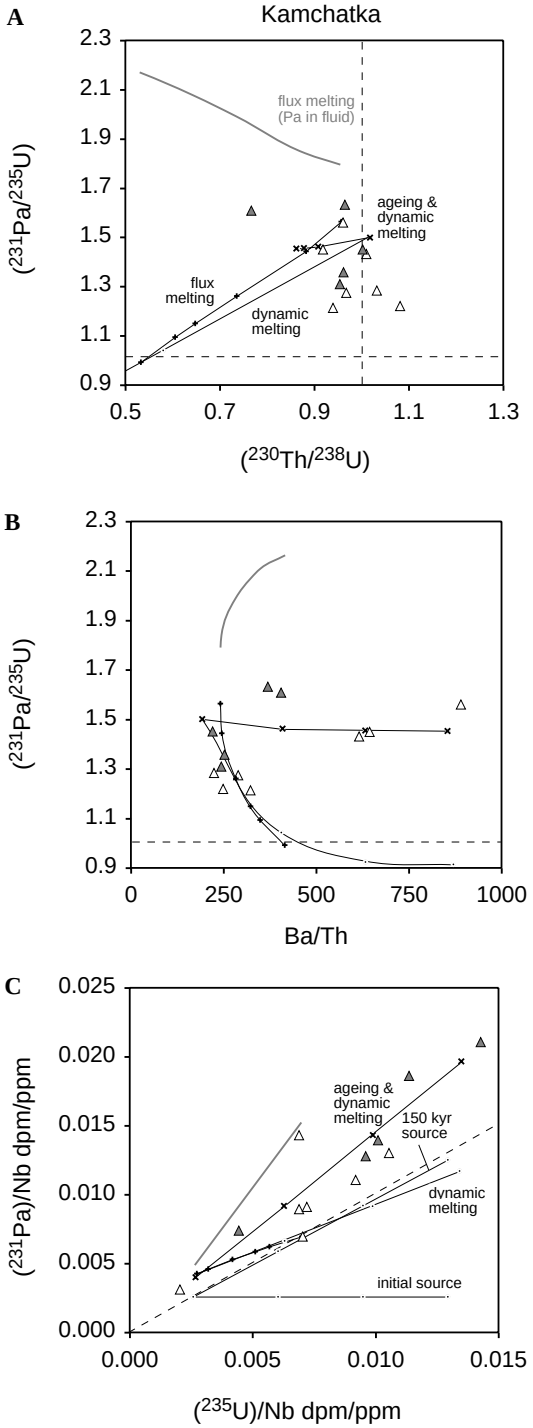

Fig. 17. Plots of (A) (^{231}Pa/^{235}U) versus (^{230}Th/^{238}U), (B) (^{231}Pa/^{235}U) versus Ba/Th, and (C) (^{231}Pa)/Nb versus (^{235}U)/Nb for Kamchatka along with melting models as illustrated in Fig. 7 (input parameters are given in Tables 2 and 3). Shaded symbols are for samples from the Eastern Volcanic Front whereas the open symbols are samples from the Central Kamchatka Depression. Data from Table 1 and selected data from Dosseto et al. (2003) for which ^{226}Ra and Ba concentration data were available in addition to ^{231}Pa.

that the ^{231}Pa–^{235}U system will have virtually returned to secular equilibrium as illustrated on the Nb-normalised diagram in Fig. 17C and the end result is that the

ageing + dynamic melting produces a shallower trend in Figs. 17A and B but a steeper one in Fig. 17C which passes through the majority of data. In contrast, neither the dynamic melting without ageing or flux melting models can produce sufficiently steep trends in Fig. 17C.

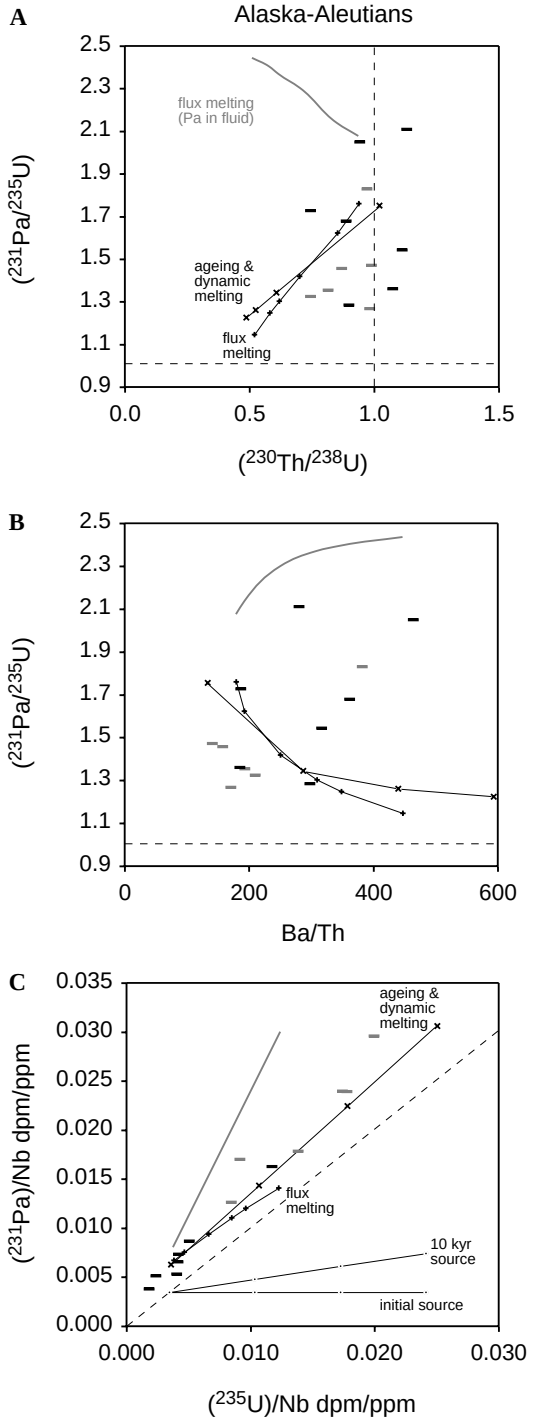

Fig. 18. Plots of (A) (^{231}Pa/^{235}U) versus (^{230}Th/^{238}U), (B) (^{231}Pa/^{235}U) versus Ba/Th, and (C) (^{231}Pa)/Nb versus (^{235}U)/Nb for the Alaska-Aleutian arc along with melting models as illustrated in Fig. 7 (input parameters are given in Tables 2 and 3). Note that due to the reduced effect of only 10 kyr ageing, only the dynamic melting + ageing models are shown for clarity. Black dashes are samples from the continental Alaska segment of the arc whereas the grey dashes are for samples from the oceanic Aleutian sector. Data from Table 1.

A.8. Alaska-Aleutians

The Alaska-Aleutian arc was one of the first in which it has been suggested that partial melting has a significant effect upon ^{230}Th–^{238}U systematics (George et al., 2003) and the new ^{231}Pa data allow for further investigation of melting processes here. Furthermore, the arc spans across continental and oceanic crust and there is a smooth progression in a number of tectonic and geochemical variables along the arc (George et al., 2003). However, recent geophysical studies have suggested that the depth to Moho may remain relatively constant along most of the arc (Fliedner and Klemperer, 2000). The continental Alaskan lavas generally have (^{231}Pa/^{235}U) higher than those of their oceanic Aleutian counterparts in Fig. 18. Finally, there is also a rear-arc volcano, Bogoslof, which allows for comparison with the arc front and intriguingly, the (^{231}Pa/^{235}U) ratio of our sample from this island is significantly higher than that obtained from the neighbouring arc front volcanoes of Akutan and Seguam (see Table 1), analogous to the variation observed amongst volcanoes from Sumbawa in the Sunda arc.

Another attribute of the Alaska-Aleutian arc is that the near horizontal base to the U–Th isotope array suggests that the time since fluid U addition can be modelled as close to zero (George et al., 2003), and dynamic melting and ageing + dynamic melting models are virtually indistinguishable if the duration of ageing is $\leqslant$10 kyr. In the (^{231}Pa/^{235}U) versus (^{230}Th/^{238}U) plot (Fig. 18A), the Alaska-Aleutian data form a scattered array and the range in (^{231}Pa/^{235}U) ratios can be broadly matched by both the (ageing +) dynamic melting and flux melting models. In Fig. 18B, the data form a positive array in the plot of (^{231}Pa/^{235}U) against Ba/Th which cannot be simulated by either of the models illustrated. However, Ba/Th ratios do not behave as simply in this arc as in many others because they are significantly influenced by the high and variable Ba contents of the subducting sediments (George et al., 2003). Fig. 18C shows that it is still possible to broadly replicate the slope of the data on the Nb-normalised diagram even when the ageing since fluid U addition is kept to a minimum. In detail, the subduction rate changes progressively along the arc due to the oblique angle of convergence of the Pacific plate. Regrettably, there is no systematic variation in (^{231}Pa/^{235}U) ratios along the arc to mirror this variation, as would be expected if subduction rate were the only variable controlling the extent of ^{231}Pa in-growth during partial melting.

References

Blundy, J.D., Robinson, J.A., Wood, B.J., 1998. Heavy REE are compatible in clinopyroxene on the spinel lherzolite solidus. *Earth Planet. Sci. Lett.* **160**, 493–504.

Blundy, J., Wood, B., 2003. Mineral–melt partitioning of Uranium, Thorium and their daughters. In: Bourdon, B., Henderson, G.M., Lundstrom, C.C., Turner, S.P. (Eds.), *Uranium-series Geochemistry*. *Rev. Mineral. Geochem.* **52**, 59–123.

Bourdon, B., Sims, K.W.W., 2003. U-series constraints on intraplate basaltic magmatism. In: Bourdon, B., Henderson, G.M., Lundstrom, C.C., Turner, S.P. (Eds.), *Uranium-series Geochemistry*. *Rev. Mineral. Geochem.* **52**, 1–21.

Bourdon, B., Turner, S., Allègre, C., 1999. Melting dynamics beneath the Tonga–Kermadec island arc inferred from ^{231}Pa–^{235}U systematics. *Science* **286**, 2491–2493.

Bourdon, B., Turner, S., Dosseto, A., 2003a. Dehydration and partial melting in subduction zones: constraints from U-series disequilibria. *J. Geophys. Res.* **108**, 2291. doi:10.1029/2002JB001839.

Bourdon, B., Turner, S., Henderson, G.M., Lundstrom, C.C., 2003b. Introduction to Uranium-series geochemistry. In: Bourdon, B., Henderson, G.M., Lundstrom, C.C., Turner, S.P. (Eds.), *Uranium-series Geochemistry*. *Rev. Mineral. Geochem.* **52**, 1–21.

Brémond d'Ars, MJ., Jaupart, C., Sparks, R.S.J., 1995. Distribution of volcanoes in active margins. *J. Geophys. Res.* **100**, 20421–20432.

Brenan, J.M., Shaw, H.F., Ryerson, F.J., Phinney, D.L., 1995. Mineral-aqueous fluid partitioning of trace elements at 900 °C and 2.0 GPa: constraints on the trace element chemistry of mantle and deep crustal fluids. *Geochim. Cosmochim. Acta* **59**, 3331–3350.

Brodholt, J.P., Batiza, R., 1989. Global systematics of unaveraged mid-ocean ridge basalt compositions: comment on "Global correlations of ocean ridge basalt chemistry with axial depth and crustal thickness" by E.M. Klein and C.H. Langmuir. *J. Geophys. Res.* **94**, 4231–4239.

Class, C., Miller, S.L., Goldstein, S.L., Langmuir, C.L., 2000. Distinguishing melt and fluid subduction components in Umnak volcanics. *Geochem. Geophys. Geosyst.* **1**. doi:10.1029/1999GC000010.

Clift, P., Vannucchi, P., 2004. Controls on tectonic accretion versus erosion in subduction zones: implications for the origin and recycling of the continental crust. *Rev. Geophys.* **42**. doi:10.1029/2003RG000127.

Conder, J.A., Wiens, D.A., Morris, J., 2002. On the decompression melting structure at volcanic arcs and back-arc spreading centers. *Geophys. Res. Lett.* **29**. doi:10.1029/2002GL015390.

Crawford, A.J., Briqueu, L., Laporte, C., Hasenaka, T., 1995. Coexistence of Indian and Pacific ocean upper mantle reservoirs beneath the central New Hebrides island arc. In: Taylor, B., Natlund, J. (Eds.), *Active Margins and Marginal Basins of the Western Pacific*. American Geophysical Union Geophysical Monograph **88**, 199–217.

Dosseto, A., Bourdon, B., Joron, J.L., Dupré, B., 2003. U–Th–Pa–Ra study of the Kamchatka arc: new constraints on the genesis of arc lavas. *Geochim. Cosmochim. Acta* **67**, 2857–2877.

Eggins, S.M., 1993. Origin and differentiation of picritic arc magmas, Ambae (Aoba), Vanuatu. *Contrib. Mineral. Petrol.* **114**, 79–100.

Ellam, R.M., Hawkesworth, C.J., 1988. Elemental and isotope variations in subduction related basalts: evidence for a three component model. *Contrib. Mineral. Petrol.* **98**, 72–80.

Elliott, T., 1997. Fractionation of U and Th during mantle melting; a reprise. *Chem. Geol.* **139**, 165–183.

Elliott, T., Plank, T., Zindler, A., White, W., Bourdon, B., 1997. Element transport from slab to volcanic front at the Mariana arc. *J. Geophys. Res.* **102**, 14991–15019.

Elliott, T., Heumann, A., Koetsier, G., 2001. U-series constraints on melting beneath the Marianas. In: *Intra-oceanic Subduction Systems: Tectonic and Magmatic Processes*. Geol. Soc. Lond. Abstr.

Elkins Tanton, L.T., Grove, T.L., Donnelly-Nolan, J., 2001. Hot, shallow mantle melting under the Cascades volcanic arc. *Geology* **29**, 631–634.

England, P., Engdahl, R., Thatcher, W., 2004. Systematic variation in the depths of slabs beneath arc volcanoes. *Geophys. J. Int.* **156**, 377–408.

Feineman, M.D., DePaolo, D.J., 2000. Steady-state ^{226}Ra/^{230}Th disequilibrium in mantle minerals: implications for melt transport rates in island arcs. *Earth Planet. Sci. Lett.* **215**, 339–355.

Fliedner, M.M., Klemperer, S.L., 2000. Crustal structure transition from oceanic arc to continental arc, eastern Aleutian Islands and Alaska Peninsula. *Earth Planet. Sci. Lett.* **179**, 567–579.

Furukawa, F., 1993. Magmatic processes under arcs and formation of the volcanic front. *J. Geophys. Res.* **98**, 8309–8319.

Gaetani, G.A., Grove, T.L., 1998. The influence of water on melting of mantle peridotite. *Contrib. Mineral. Petrol.* **131**, 323–346.

Geist, E.L., Vallier, T.L., Scholl, D.W., 1994. Origin, transport, and emplacement of an exotic island-arc terrane exposed in eastern Kamchatka, Russia. *Geol. Soc. Am. Bull.* **106**, 1182–1194.

George, R., Turner, S., Hawkesworth, C., Morris, J., Nye, C., Ryan, J., Zheng, S.-H., 2003. Melting processes and fluid and sediment transport rates along the Alaska-Aleutian arc from an integrated U–Th–Ra–Be isotope study. *J. Geophys. Res.* **108**, 2252. doi:10.1029/2002JB001916.

George, R., Reagan, M., Turner, S., Gill, J., Bourdon, B., 2004. Comment on "Steady-state ^{226}Ra/^{230}Th disequilibrium in mantle minerals: implications for melt transport rates in island arcs" by M.D. Feineman and D.J. DePaolo [Earth Planet. Sci. Lett. 215 (2003) 339–355]. *Earth Planet. Sci. Lett.* **228**, 563–567.

George, R., Turner, S., Morris, J., Plank, T., Hawkesworth, C., Ryan, J., 2005. Pressure–temperature–time paths of sediment recycling beneath the Tonga–Kermadec arc. *Earth Planet. Sci. Lett.* **233**, 195–211.

Gerbe, M.-C., Gourgaud, A., Sigmarsson, O., Harmon, R.S., Joron, J.-L., Provost, A., 1992. Mineralogical and geochemical evolution of the 1982–1983 Galunggung eruption (Indonesia). *Bull. Volcanol.* **54**, 284–298.

Gerya, T.V., andYuen, D.A., 2003. Rayleigh–Taylor instabilities from hydration and melting propel 'cold plumes' at subduction zones. *Earth Planet. Sci. Lett.* **212**, 47–62.

Halliday, A.N., Lee, D.-C., Tommasini, S., Davies, G.R., Paslick, C.R., Fitton, J.G., James, D.E., 1995. Incompatible trace elements in OIB and MORB and source enrichment in the sub-oceanic mantle. *Earth Planet. Sci. Lett.* **133**, 379–395.

Hamilton, W., 1979. Tectonics of the Indonesian region. USGS Prof. Pap. 1078.

Hawkesworth, C., Turner, S., Peate, D., McDermott, F., van Calsteren, P., 1997. Elemental U and Th variations in island arc rocks: implications for U-series isotopes. *Chem. Geol.* **139**, 207–222.

Heath, E., Macdonald, R., Belkin, H., Hawkesworth, C., Sigurdsson, H., 1998. Magma genesis at Soufriere volcano, St. Vincent, Lesser Antilles arc. *J. Petrol.* **39**, 1721–1764.

Hirschmann, M.M., Asimow, P.D., Ghiorso, M.S., Stolper, E.M., 1999. Calculation of peridotite partial melting form thermodynamic model of minerals and melts III. Controls on isobaric melt production and the effect of water on melt production. *J. Petrol.* **40**, 831–851.

Hofmann, A.W., Jochum, K.P., Seufert, M., andWhite, WM, 1986. Nb and Pb in oceanic basalts: new constraints on mantle evolution. *Earth Planet. Sci. Lett.* **79**, 33–45.

Honda, S., Yoshida, T., 2005. Application of the model of small-scale convection under the island arc to the NE Honshu. *Geochem. Geophys. Geosyst.* **6**. doi:10.1029/2004GC000785.

Hutchison, C.S., 1976. Indonesian active volcanic arc: K, Sr and Rb variation with depth to the Benioff zone. *Geology* **4**, 407–408.

Jarrard, R.D., 1986. Relations among subduction parameters. *Rev. Geophys.* **24**, 217–284.

Johnson, M.C., Plank, T., 1999. Dehydration and melting experiments constrain the fate of subducted sediments. *Geochem. Geophys. Geosyst.* **1**. doi:10.1029/1999GC000014.

Kepzhinskas, P., McDermott, F., Defant, M.J., Hochstaedter, A., Drummond, M.S., Hawkesworth, C.J., Koloskov, A., Maury, R.C., Bellon, H., 1997. Tace element and Sr-Nd-Pb isotopic constraints on a three-component model of Kamchatka arc petrogenesis. *Geochim. Cosmochim. Acta* **61**, 577–600.

Kincaid, C., Sacks, I.S., 1997. Thermal and dynamic evolution of the upper mantle in subduction zones. *J. Geophys. Res.* **102**, 12295–12315.

Klein, E.M., Langmuir, C.H., 1989. Local versus global correlations in ocean ridge basalt composition: a reply. *J. Geophys. Res.* **94**, 4241–4252.

Landwehr, D., Blundy, J., Chamorro-Perez, E.M., Hill, E., Wood, B.J., 2001. U-series disequilibria generated by partial melting of spinel lherzolite. *Earth. Planet. Sci. Lett.* **188**, 329–348.

Lundstrom, C.C., Sampson, D.E., Perfot, M.R., Gill, J., Williams, Q., 1999. Insights into mid-ocean ridge basalt petrogenesi; U-series disequilibria from the Siqueiros Transform, Lamont Seamounts, and East Pacific Rise. *J. Geophys. Res.* **104**, 13035–13048.

Lundstrom, C.C., 2003. Uranium-series disequilibria in Mid-ocean Ridge Basalts: observations and models of Basalt Genesis. In: Bourdon, B., Henderson, G.M., Lundstrom, C.C., Turner, S.P. (Eds.), *Uranium-series Geochemistry*. *Rev. Mineral. Geochem.* **52**, 175–214.

Macdonald, R., Hawkesworth, C.J., Heath, E., 2000. The Lesser Antilles volcanic chain: a study in arc magmatism. *Earth Sci. Rev.* **49**, 1–76.

McDermott, F., Defant, M.J., Hawkesworth, C.J., Maury, R.C., 1993. Isotope and trace element evidence for three component mixing in the genesis of North Luzon arc lavas (Philippines). *Contrib. Mineral. Petrol.* **113**, 9–23.

McDermott, F., Hawkesworth, C., 1991. Th, Pb, and Sr isotope variations in young island arc volcanics and oceanic sediments. *Earth Planet. Sci. Lett.* **104**, 1–15.

McKenzie, D., 1985. ^{230}Th–^{238}U disequilibrium and the melting process beneath ridge axes. *Earth Planet. Sci. Lett.* **72**, 149–157.

Parkinson, I.J., Arculus, R.J., 1999. The redox state of subduction zones: insights from arc-peridotites. *Chem. Geol.* **160**, 409–423.

Pearce, J.A., Parkinson, I.J., 1993. Trace element models for mantle melting: application to volcanic arc petrogenesis. *J. Geol. Soc. Lond.* **76**, 373–403.

Peate, D.W., Hawkesworth, C.J., 2005. U series disequilibria: insights into mantle melting and the timescales of magma differentiation. *Rev. Geophys.* **43**. doi:10.1029/2004RG000154.

Peate, D.W., Kokfelt, T.F., Hawkesworth, C.J., van Calsteren, P.W., Hergt, J.M., Pearce, J.A., 2001. U-series isotope data on Lau Basin glasses: the role of subduction-related fluids during melt generation in back-arc basins. *J. Petrol.* **42**, 1449–1470.

Pickett, D.A., Murrell, M.T., 1997. Observations of ^{231}Pa/^{235}U disequilibrium in volcanic rocks. *Earth Planet. Sci. Lett.* **148**, 259–271.

Plank, T., Langmuir, C.H., 1988. An evaluation of the global variations in the major element chemistry of arc basalts. *Earth Planet. Sci. Lett.* **90**, 349–370.

Plank, T., Langmuir, C.H., 1998. The chemical composition of subducting sediment and its consequences for the crust and mantle. *Chem. Geol.* **145**, 325–394.

Plank, T., 2005. Constraints from Thorium/Lanthanum on sediment recycling at subduction zones and the evolution of the continents. *J. Petrol.* **46**, 921–944.

Poli, S., Schmidt, M.W., 1995. H_2O transport and release in subduction zones: experimental constraints on basaltic and andesitic systems. *J. Geophys. Res.* **100**, 22299–22314.

Regelous, M., Collerson, K.D., Ewart, A., Wendt, J.I., 1997. Trace element transport rates in subduction zones: evidence from Th, Sr and Pb isotope data for Tonga–Kermadec arc lavas. *Earth Planet. Sci. Lett.* **150**, 291–302.

Regelous, M., Turner, S., Elliott, T.R., Rostami, K., Hawkesworth, C.J., 2004. Rapid measurement of femtogram quantities of Protactinium in silicate rock samples by multicollector inductively coupled plasma mass spectrometry. *Anal. Chem.* **76**, 3584–3589.

Salters, V.J.M., Stracke, A., 2004. Composition of the depleted mantle. *Geochem. Geophys. Geosyst.* **5**. doi:10.1029/2003GC000597.

Schmidt, M.W., Poli, S., 1998. Experimentally based water budgets for dehydrating slabs and consequences for arc magma generation. *Earth Planet. Sci. Lett.* **163**, 361–379.

Shimizu, N., Arculus, R.J., 1975. Rare earth element concentrations in a suite of basabitoids and alkali olivine basalts from Grenada, Lesser Antilles. *Contrib. Mineral. Petrol.* **50**, 231–240.

Sigmarsson, O., Chmeleff, J., Morris, J., Lopez-Escobar, L., 2002. Origin of ^{226}Ra–^{230}Th disequilibria in arc lavas from southern Chile and magma transfer time. *Earth Planet. Sci. Lett.* **196**, 189–196.

Sisson, T.W., Bronto, S., 1998. Evidence for pressure-release melting beneath magmatic arcs from basalt at Galunggung, Indonesia. *Nature* **391**, 883–886.

Spiegelman, M., Elliott, T., 1993. Consequences of melt transport for uranium series disequilibrium. *Earth Planet. Sci. Lett.* **118**, 1–20.

Stolper, E., Newman, S., 1994. The role of water in the patrogenesis of Mariana trough magmas. *Earth Planet. Sci. Lett.* **121**, 293–325.

Tatsumi, Y., Hamilton, D.L., Nesbitt, R.W., 1986. Chemical characteristics of fluid phase released from a subducted lithosphere and origin of arc magmas: evidence from high-pressure experiments and natural rocks. *J. Volcanol. Geotherm. Res.* **29**, 293–309.

Taylor, F.W., Bevis, M.G., Schultz, B.E., Kuang, D., Recy, J., Calmant, S., Charley, D., Regnier, M., Perin, B., Jackson, M., Reichenfeld, C., 1995. Geodetic measurements of convergence at the New Hebrides island arc indicate arc fragmentation caused by an impinging aseismic ridge. *Geology* **23**, 1011–1014.

Taylor, B., Martinez, F., 2003. Back-arc basin basalt systematics. *Earth Planet. Sci. Lett.* **201**, 481–497.

Thomas, R.B., Hirschmann, M.M., Cheng, H., Reagan, M.K., Edwards, R.L., 2002. (^{231}Pa/^{235}U)–(^{230}Th/^{238}U) of young mafic volcanic rocks from Nicaragua and Costa Rica and the influence of flux melting on U-series systematics of arc lavas. *Geochim. Cosmochim. Acta* **66**, 4287–4309.

Turner, S., Hawkesworth, C., van Calsteren, P., Heath, E., Macdonald, R., Black, S., 1996. U-series isotopes and destructive plate margin magma genesis in the Lesser Antilles. *Earth Planet. Sci. Lett.* **142**, 191–207.

Turner, S., Hawkesworth, C., Rogers, N., Bartlett, J., Worthington, T., Hergt, J., Pearce, J., Smith, I., 1997. ^{238}U–^{230}Th disequilibria, magma petrogenesis and flux rates beneath the depleted Tonga–Kermadec island arc. *Geochim. Cosmochim. Acta* **61**, 4855–4884.

Turner, S., McDermott, F., Hawkesworth, C., Kepezhinskas, P., 1998. A U-series study of lavas from Kamchatka and the Aleutians: constraints on source composition and melting processes. *Contrib. Mineral. Petrol.* **133**, 217–234.

Turner, S.P., Peate, D.W., Hawkesworth, C.J., Eggins, S.M., Crawford, A.J., 1999. Two mantle domains and the time scales of fluid transfer beneath the Vanuatu arc. *Geology* **27**, 963–966.

Turner, S., Bourdon, B., Hawkesworth, C., Evans, P., 2000. ^{226}Ra–^{230}Th evidence for multiple dehydration events, rapid melt ascent and the time scales of differentiation beneath the Tonga–Kermadec island arc. *Earth Planet. Sci. Lett.* **179**, 581–593.

Turner, S., Foden, J., 2001. U, Th and Ra disequilibria, Sr, Nd and Pb isotope and trace element variations in Sunda arc lavas: predominance of a subducted sediment component. *Contrib. Mineral. Petrol.* **142**, 43–57.

Turner, S., Evans, P., Hawkesworth, C., 2001. Ultra-fast source-to-surface movement of melt at island arcs from ^{226}Ra–^{230}Th systematics. *Science* **292**, 1363–1366.

Turner, S., Bourdon, B., Gill, J., 2003. Insights into magma genesis at convergent margins from U-series isotopes. In: Bourdon, B., Henderson, G.M., Lundstrom, C.C., Turner, S.P. (Eds.), *Uranium-series Geochemistry*. *Rev. Mineral. Geochem.* **52**, 255–315.

Turner, S., Black, S., Berlo, K., 2004. ^{210}Pb–^{226}Ra and ^{228}Ra–^{232}Th systematics in young arc lavas: implications for magma degassing and ascent rates. *Earth Planet. Sci. Lett.* **227**, 1–16.

van Keken, P.E., Kiefer, B., Peacock, S.M., 2002. High-resolution models of subduction zones: implications for mineral dehydration reactions and the transport of water into the deep mantle. *Geochem. Geophys. Geosyst.* **3**. doi:10.1029/2001GC000256.

Williams, R.W., Gill, J.B., 1989. Effects of partial melting on the uranium decay series. *Geochim. Cosmochim. Acta* **53**, 1607–1619.

Woodhead, J.D., 1989. Geochemistry of the Mariana arc (western Pacific): source composition and processes. *Chem. Geol.* **76**, 1–24.

Yogodzinsky, G.M., Lees, J.M., Churikova, T.G., Dorendorf, F., Wörner, G., Volynets, O.N., 2001. Geochemical evidence for the melting of subducting oceanic lithosphere at plate edges. *Nature* **409**, 500–504.

Zellmer, G.F., Hawkesworth, C.J., Sparks, R.S.J., Thomas, L.E., Harford, C.L., Brewer, T.S., Loughlin, S.C., 2003. Geochemical evolution of the Soufrière Hills volcano, Montserrat, Lesser Antilles volcanic arc. *J. Petrol.* **44**, 1349–1374.